ELSEVIER

Comput. Methods Appl. Mech. Engrg. 190 (2001) 3293–3323

Computer methods in applied mechanics and engineering

www.elsevier.com/locate/cma

Cam-Clay plasticity, Part IV: Implicit integration of anisotropic bounding surface model with nonlinear hyperelasticity and ellipsoidal loading function

Ronaldo I. Borja *, Chao-Hua Lin, Francisco J. Montáns

Department of Civil and Environmental Engineering, Stanford University, Stanford, CA 94305-4020, USA

Received 16 February 2000

Abstract

This paper describes a fully implicit stress-point integration algorithm for a class of anisotropic bounding surface plasticity models with ellipsoidal loading function. The plasticity model is coupled with a nonlinear hyperelastic model to ensure that the elastic component of the combined model is energy-conserving. A key feature of the integration algorithm for the combined model is a return mapping in strain space, which allows fully implicit integration and consistent linearization of the constitutive equations. For this class of bounding surface models the consistency condition on the bounding surface is shown to be mathematically equivalent to the consistency condition on the loading surface, thus allowing practically all attributes of the standard return mapping algorithm of classical plasticity theory to be carried over to the bounding surface theory with little modification. As a specific example, the infinitesimal version of modified Cam-Clay theory is used to represent the bounding surface model, and an exponential function is used to interpolate the plastic modulus on the loading surface. Isoerror maps are generated describing the accuracy of the integration algorithm on the stress-point level. Finally, a boundary-value problem involving a strip footing on lightly overconsolidated clay is analyzed to demonstrate the robustness of the algorithm in a finite element setting.

1. Introduction

One of the most compelling problems in geomechanics is the description of the mechanical behavior of soils under cyclic loading conditions. For loading histories with repetitive loading action the mechanical behavior of soils is dominated by hysteretic motion [1–3]. Thus, proper account must be taken of material anisotropy as well as the accompanying stiffness degradation and pore pressure buildup (for saturated soils) during cyclic loading. Widely used plasticity models developed to capture these complex soil responses generally fall under the categories of nested surface plasticity [4–8] and bounding surface plasticity models [9–15]. While neither class of models has any distinct advantage over the other from an analytical standpoint, the bounding surface formulation arguably lends itself to simpler numerical implementation compared to the nested yield surface formulation. Since simplicity is a critical aspect of large-scale mathematical modeling, the bounding surface formulation is chosen in this paper to account for anisotropy as it relates to the response of soils to cyclic loading.

Classical rate-independent plasticity models require a numerical integration strategy to allow a description of the evolution of the material responses over a finite load increment [16–18]. In this

* Corresponding author. Fax: +650-723-7514.
E-mail address: borja@cive.stanford.edu (R.I. Borja).

0045-7825/01/$ - see front matter
PII: S0045-7825(00)00301-7

regard, return maps based on the implicit backward scheme (termed "catching-up" algorithm in [19]) are now routinely used in many computer codes. This algorithm is a member of a wider class of return mapping algorithms based on the generalized midpoint rule, described in [20], which is shown to be nonlinearly stable (A-contractive) for $\alpha \geqslant 1/2$. Traditionally, return maps are done in stress space under the hypothesis of constant elastic moduli; however, with stress-dependent elastic moduli, such as those arising from nonlinear hyperelasticity, return maps can be done just as conveniently in strain space [21–23].

Despite their widespread use in classical rate-independent plasticity, return maps based on the implicit backward scheme have yet to address the computational needs of bounding surface-type models. This may be attributed to the indirect nature of return maps within the context of bounding surface formulation owing to the internal structure of the constitutive model itself. For one, the consistency condition is invoked on the bounding surface through the motion of an 'image' stress point, which generally does not coincide with the stress point itself. Furthermore, there is a lack of a yield surface on which return maps may be performed, only a 'loading' surface where the consistency condition is not invoked in the first place. Still, sporadic efforts have been made in recent years to cast bounding surface-type models within the framework of return mapping algorithm [24–27].

This paper reformulates a class of rate-independent bounding surface plasticity models to make them more amenable to implicit integration and consistent linearization with Newton's method. The version of the bounding surface model of interest uses a radial mapping rule to define the image stress point on the bounding surface [10]. A key feature exploited in this paper is the choice of a loading surface that is homologous to the bounding surface, which effectively allows the former surface to be treated essentially as a yield surface. As a result, the consistency condition on the bounding surface becomes equivalent to the consistency condition on the loading surface, and hence practically all features of the standard return mapping algorithm are applied to the bounding surface model with little modification.

As a specific example, the infinitesimal version of modified Cam-Clay theory of critical state soil mechanics, presented in [23], is used to represent the bounding surface model. Cam-Clay models are capable of representing many important features of soil behavior such as pressure sensitivity, hardening response with plastic volumetric compaction, softening response with plastic dilation, and coupled volumetric–deviatoric plastic deformations [28–33]. However, it is not capable of replicating hysteretic action from cyclic loading. In this paper we enhance a Cam-Clay model to incorporate plastic deformation beneath the yield surface through an anisotropic bounding surface formulation that allows hysteretic action, stiffness degradation, and even pore pressure buildup (for the case of saturated soils) to be captured during cyclic loading. The resulting bounding surface model is then coupled with an energy-conserving nonlinear hyperelastic model characterized by pressure-dependent elastic bulk and shear moduli [34,35].

The order of presentation goes as follows. Section 2 describes the general theory of ellipsoidal yield function with a linear combination of isotropic and kinematic hardening, based on which a bounding surface theory is reformulated in Section 3. Section 4 casts a Cam-Clay model within the bounding surface framework, and Section 5 discusses the well-posedness of this combined model in a continuum setting. The discrete formulation is presented in Section 6, followed by a discussion of some selected numerical examples in Section 7. As for notations and symbols, bold-face letters denote matrices and vectors; the symbol '$\cdot$' denotes an inner product of two vectors (e.g. $\boldsymbol{a} \cdot \boldsymbol{b} = a_i b_i$), or a single contraction of adjacent indices of two tensors (e.g. $\boldsymbol{c} \cdot \boldsymbol{d} = c_{ij} d_{jk}$); the symbol ':' denotes an inner product of two second-order tensors (e.g. $\boldsymbol{c} : \boldsymbol{d} = c_{ij} d_{ij}$), or a double contraction of adjacent indices of tensors of rank two and higher (e.g. $\boldsymbol{C} : \boldsymbol{\epsilon}^{\mathrm{e}} = C_{ijkl} \epsilon^{\mathrm{e}}_{kl}$).

2. Theory of ellipsoidal yield surface

The general equation of a translated ellipsoid in principal stress space that has one of its axes parallel to the hydrostatic axis is

$$\mathscr{F} = \|\boldsymbol{s} - \boldsymbol{\alpha}_s\|^2 + c^2 (p - \alpha_p)^2 - r^2 = 0, \tag{2.1}$$

where

$$p = \frac{1}{3}\mathrm{tr}(\boldsymbol{\sigma}), \quad \boldsymbol{s} = \boldsymbol{\sigma} - p\mathbf{1}, \quad \alpha_p = \frac{1}{3}\mathrm{tr}(\boldsymbol{\alpha}), \quad \boldsymbol{\alpha}_s = \boldsymbol{\alpha} - \alpha_p\mathbf{1}. \tag{2.2}$$

Here, $\boldsymbol{\sigma}$ is the Cauchy stress tensor, $\boldsymbol{\alpha}$ the backstress tensor, $\mathbf{1}$ the Kronecker delta tensor, r the radius of the ellipsoid representing the maximum value of the tensor norm $\|\boldsymbol{s} - \boldsymbol{\alpha}_s\|$, and c is the axis ratio of the ellipsoid. Clearly, a translated cylinder in principal stress space can be recovered from (2.1) when $c = 0$.

Alternately, a fourth-order tensor $\boldsymbol{M}$ may be defined as

$$\boldsymbol{M} = \left(\boldsymbol{I} - \frac{1}{3}\mathbf{1}\otimes\mathbf{1}\right) + \left(\frac{c}{3}\right)^2 \mathbf{1}\otimes\mathbf{1}, \tag{2.3}$$

where $\boldsymbol{I}$ is the rank-four identity tensor with components $\boldsymbol{I}_{ijkl} = (1/2)(\delta_{ik}\delta_{jl} + \delta_{il}\delta_{jk})$, and $(\mathbf{1}\otimes\mathbf{1})_{ijkl} = \delta_{ij}\delta_{kl}$. The ellipsoid can thus be written in the more compact form

$$\mathscr{F} = \boldsymbol{\xi} : \boldsymbol{M} : \boldsymbol{\xi} - r^2 = 0, \quad \boldsymbol{\xi} = \boldsymbol{\sigma} - \boldsymbol{\alpha}. \tag{2.4}$$

If the axis ratio c is constant, then $\boldsymbol{M}$ is constant, and the ellipsoid retains its shape. Without much loss of generality, this paper considers the case where c is constant. The geometry of the ellipsoid in principal stress space is shown in Fig. 1.

Consider now a convex elastic domain $\boldsymbol{E}$ defined by the ellipsoid $\mathscr{F}$ in the Cauchy stress space $\boldsymbol{\sigma}$:

$$\boldsymbol{E} = \{(\boldsymbol{\sigma}, r) \in S \times R^1 \mid \mathscr{F}(\boldsymbol{\sigma}, r) \leqslant 0\}, \tag{2.5}$$

where S is the space of symmetric rank-two tensors, and r is a stress-like plastic internal variable characterizing the hardening response of the material. Constraining c to be constant implies that the size of the ellipsoid is determined solely by the magnitude of the scalar quantity r. Assuming that the constitutive equation is expressed in terms of a free energy function $\Psi(\boldsymbol{\epsilon}^{\mathrm{e}}, \theta)$, where $\boldsymbol{\epsilon}^{\mathrm{e}}$ is the elastic component of the infinitesimal strain tensor $\boldsymbol{\epsilon}$, and θ denotes a strain-like plastic variable conjugate to r, we have

$$\boldsymbol{\sigma} = \frac{\partial\Psi(\boldsymbol{\epsilon}^{\mathrm{e}}, \theta)}{\partial\boldsymbol{\epsilon}^{\mathrm{e}}}, \quad r = -\frac{\partial\Psi(\boldsymbol{\epsilon}^{\mathrm{e}}, \theta)}{\partial\theta}. \tag{2.6}$$

As an example, $\theta = \epsilon_v^{\mathrm{p}} = \mathrm{tr}(\boldsymbol{\epsilon}^{\mathrm{p}})$ is a possible candidate for θ, where ϵ_v^{p} is the plastic volumetric strain. Eq. $(2.6)_1$ is characteristic of a hyperelastic response.

Next we define a plastic potential function $\mathscr{G}$ such that the evolutions of $\boldsymbol{\epsilon}^{\mathrm{p}}$ and θ are given by

$$\dot{\boldsymbol{\epsilon}}^{\mathrm{p}} = \dot{\gamma}\frac{\partial\mathscr{G}(\boldsymbol{\sigma}, r)}{\partial\boldsymbol{\sigma}}, \quad \dot{\theta} = \dot{\gamma}\frac{\partial\mathscr{G}(\boldsymbol{\sigma}, r)}{\partial r}, \tag{2.7}$$

where $\dot{\gamma}$ is a plastic consistency parameter satisfying the Kuhn–Tucker complementary conditions

$$\dot{\gamma} \geqslant 0, \quad \mathscr{F}(\boldsymbol{\sigma}, r) \leqslant 0, \quad \dot{\gamma}\mathscr{F}(\boldsymbol{\sigma}, r) = 0. \tag{2.8}$$

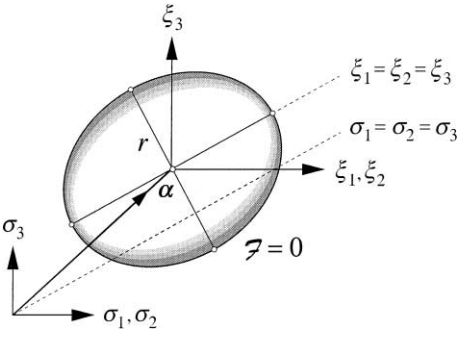

Fig. 1. Translated ellipsoid in principal stress space.

Associative plasticity and hardening implies that $\partial\mathscr{F}/\partial\boldsymbol{\sigma} = \partial\mathscr{G}/\partial\boldsymbol{\sigma}$ and $\partial\mathscr{F}/\partial r = \partial\mathscr{G}/\partial r$. For nonassociative plasticity a simple model can be constructed by setting

$$\boldsymbol{f} = \frac{\partial\mathscr{F}}{\partial\boldsymbol{\sigma}} = 2\boldsymbol{M} : \boldsymbol{\xi}, \quad \boldsymbol{g} = \frac{\partial\mathscr{G}}{\partial\boldsymbol{\sigma}} = 2\boldsymbol{M}^* : \boldsymbol{\xi}, \tag{2.9}$$

where $\boldsymbol{M}^*$ is a fourth-order tensor defined similarly to $\boldsymbol{M}$ in (2.3) but based on a different axis ratio $c^* \neq c$. In this case, plasticity is nonassociative only in the isotropic sense but remains associative in the deviatoric sense.

Assume now that the backstress tensor $\boldsymbol{\alpha}$ evolves according the expression

$$\dot{\boldsymbol{\alpha}} = \|\dot{\boldsymbol{\alpha}}\|\boldsymbol{\mu}, \quad \|\boldsymbol{\mu}\| = 1, \tag{2.10}$$

where $\boldsymbol{\mu}$ is a unit tensor defining the direction of the translation of $\mathscr{F}$. If $\dot{r} = 0$, then $\mathscr{F}$ hardens kinematically, and

$$\dot{\boldsymbol{\alpha}} = \frac{\boldsymbol{f} : \dot{\boldsymbol{\sigma}}}{\boldsymbol{f} : \boldsymbol{\mu}}\boldsymbol{\mu}. \tag{2.11}$$

On the other hand, if $\dot{\boldsymbol{\alpha}} = \boldsymbol{0}$, then $\mathscr{F}$ hardens isotropically, and

$$\dot{r} = -\dot{\gamma}\Psi_{,\theta\theta}\frac{\partial\mathscr{G}}{\partial r}, \quad \Psi_{,\theta\theta} = \frac{\partial^2\Psi(\boldsymbol{\epsilon}^{\mathrm{e}}, \theta)}{\partial\theta^2}. \tag{2.12}$$

If $\mathscr{F}$ hardens both isotropically and kinematically, we can combine the two types of hardening linearly through a constant parameter $\zeta \in [0, 1]$ and write

$$\dot{r} = -\zeta\dot{\gamma}\Psi_{,\theta\theta}\frac{\partial\mathscr{G}}{\partial r}, \quad \dot{\boldsymbol{\alpha}} = (1-\zeta)\frac{\boldsymbol{f} : \dot{\boldsymbol{\sigma}}}{\boldsymbol{f} : \boldsymbol{\mu}}\boldsymbol{\mu}. \tag{2.13}$$

Clearly, the case $\zeta = 0$ results in a kinematically hardening response, whereas $\zeta = 1$ gives an isotropically hardening response.

Let us define the Hessian tensor

$$\boldsymbol{c}^{\mathrm{e}} = \frac{\partial^2\Psi(\boldsymbol{\epsilon}^{\mathrm{e}}, \theta)}{\partial\boldsymbol{\epsilon}^{\mathrm{e}}\partial\boldsymbol{\epsilon}^{\mathrm{e}}} \tag{2.14}$$

representing the symmetric, positive-definite tensor of tangential elastic moduli. The consistency condition, $\dot{\mathscr{F}} = 0$, gives

$$\dot{\mathscr{F}} = \boldsymbol{f} : (\dot{\boldsymbol{\sigma}} - \dot{\boldsymbol{\alpha}}) + \frac{\partial\mathscr{F}}{\partial r}\dot{r} = 0. \tag{2.15}$$

Substituting (2.13), we get

$$\dot{\mathscr{F}} = \boldsymbol{f} : \dot{\boldsymbol{\sigma}} - \dot{\gamma}\mathscr{H} = 0, \quad \mathscr{H} = \frac{\partial\mathscr{F}}{\partial r}\Psi_{,\theta\theta}\frac{\partial\mathscr{G}}{\partial r}. \tag{2.16}$$

Note that the parameter ζ does not appear in the consistency condition. Since $\dot{\boldsymbol{\sigma}} = \dot{\boldsymbol{\sigma}}^{\mathrm{tr}} - \dot{\gamma}\boldsymbol{c}^{\mathrm{e}} : \boldsymbol{g}$, where $\dot{\boldsymbol{\sigma}}^{\mathrm{tr}} = \boldsymbol{c}^{\mathrm{e}} : \dot{\boldsymbol{\epsilon}}$ is the trial-rate-of-stress tensor, then we can use $(2.16)_1$ to evaluate the parameter $\dot{\gamma}$ as

$$\dot{\gamma} = \frac{\boldsymbol{f} : \dot{\boldsymbol{\sigma}}^{\mathrm{tr}}}{\boldsymbol{f} : \boldsymbol{c}^{\mathrm{e}} : \boldsymbol{g} + \mathscr{H}}. \tag{2.17}$$

The continuum tangential moduli tensor takes the familiar form

$$\boldsymbol{c}^{\mathrm{ep}} = \boldsymbol{c}^{\mathrm{e}} - \frac{1}{\chi}\boldsymbol{c}^{\mathrm{e}} : \boldsymbol{g} \otimes \boldsymbol{f} : \boldsymbol{c}^{\mathrm{e}}, \quad \chi = \boldsymbol{f} : \boldsymbol{c}^{\mathrm{e}} : \boldsymbol{g} + \mathscr{H} > 0. \tag{2.18}$$

Observe that neither $\dot{\gamma}$ nor $\boldsymbol{c}^{\mathrm{ep}}$ is influenced by the translation variables ζ and $\boldsymbol{\mu}$. However, the choice of the specific translation rule and relative degree of isotropic/kinematic hardening does impact the constitutive response on reverse and cyclic loadings.

A fully symmetric formulation is obtained by taking $\mathscr{F} = \mathscr{G}$. This results in $\boldsymbol{f} = \boldsymbol{g}$ and $\partial\mathscr{F}/\partial r = \partial\mathscr{G}/\partial r$, implying symmetry in both the continuum and algorithmic tangential moduli tensors [17]. It must be emphasized that symmetry in the algorithmic tangential moduli tensor resulting from the use of return-mapping algorithms also necessitates an associated hardening derived from a free-energy function, see $(2.16)_2$. However, such a free energy function usually is not available in practice, and so the algorithmic tangential moduli tensor can be expected to be unsymmetric in the general case.

3. Theory of ellipsoidal bounding surface

Bounding surface plasticity theory is based on the notion that there exists a surface that encloses all possible states in stress space, and that plastic yielding inside this surface is possible through some form of mapping of the stress point onto its image on the bounding surface. The most widely used mapping rule for soil materials is radial mapping [10], which is given by the following expression:

$$\hat{\boldsymbol{\sigma}} = \boldsymbol{\sigma} + \kappa(\boldsymbol{\sigma} - \boldsymbol{\sigma}_0). \tag{3.1}$$

Here, $\boldsymbol{\sigma}$ is the stress point in question, $\hat{\boldsymbol{\sigma}}$ is its image on the bounding surface, $\boldsymbol{\sigma}_0$ the projection center, and $\kappa \geqslant 0$ is a scalar parameter relating the position of $\boldsymbol{\sigma}$ relative to $\boldsymbol{\sigma}_0$ and $\hat{\boldsymbol{\sigma}}$. Clearly, $\kappa = 0$ corresponds to $\boldsymbol{\sigma} = \hat{\boldsymbol{\sigma}}$, whereas $\kappa \to \infty$ corresponds to $\boldsymbol{\sigma} = \boldsymbol{\sigma}_0$ (see Fig. 2).

Since $\hat{\boldsymbol{\sigma}}$ lies on the bounding surface, then it must satisfy the equation for this surface. Let us use the theory of ellipsoidal surface described in the previous section and write an expression for the bounding surface as

$$F = \hat{\boldsymbol{\xi}} : \boldsymbol{M} : \hat{\boldsymbol{\xi}} - R^2 = 0, \quad \hat{\boldsymbol{\xi}} = \hat{\boldsymbol{\sigma}} - \boldsymbol{\beta}. \tag{3.2}$$

We identify F as an ellipsoid having a size R, a backstress $\boldsymbol{\beta}$, and an axis ratio c, which enters into the fourth-order tensor $\boldsymbol{M}$ through Eq. (2.3). As before, this translated ellipsoid has one of its axes parallel to the hydrostatic axis in principal stress space.

Substituting (3.1) into (3.2) gives

$$F = (1+\kappa)^2 \boldsymbol{\xi} : \boldsymbol{M} : \boldsymbol{\xi} - R^2 = 0, \tag{3.3}$$

where

$$\boldsymbol{\xi} = \boldsymbol{\sigma} - \boldsymbol{\alpha}, \quad \boldsymbol{\alpha} = \frac{\kappa\boldsymbol{\sigma}_0 + \boldsymbol{\beta}}{1+\kappa}. \tag{3.4}$$

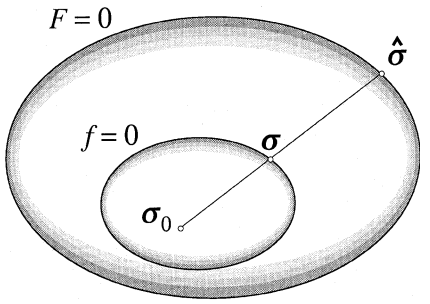

Fig. 2. Projection center, stress point, and image point.

Dividing (3.3) by $(1+\kappa)^2$ gives

$$f \equiv \frac{F}{(1+\kappa)^2} = \boldsymbol{\xi} : \boldsymbol{M} : \boldsymbol{\xi} - r^2 = 0, \quad r^2 = \left(\frac{R}{1+\kappa}\right)^2. \tag{3.5}$$

The function f is another translated ellipsoid homologous to F, which has the same axis ratio c, a reduced size r, and a backstress $\boldsymbol{\alpha}$. Since the projection center $\boldsymbol{\sigma}_0$ defines this ellipsoid, it is called the homology center. An equivalent interpretation of f is that it is the locus of all points in stress space on which κ is constant.

The function f, usually called the loading function, has properties very similar to those of the bounding function F as summarized below.

Proposition 1. *If* $F = \dot{F} = 0$, *then* $f = \dot{f} = 0$.

Proof. The result $f = 0$ if $F = 0$ follows trivially from (3.5). Taking the time-derivative of F gives

$$\dot{F} = (1+\kappa)^2 \dot{f} + 2f(1+\kappa)\dot{\kappa} = 0.$$

Since $f = 0$, it follows that $\dot{f} = 0$. This result implies that the consistency condition on F is equivalent to the consistency condition on f. □

Proposition 2. *Let* $f = F/(1+\kappa)^2$ *as defined in* (3.5). *Then*,

$$\boldsymbol{f} = \frac{\partial f}{\partial \boldsymbol{\sigma}} \quad \textit{and} \quad \hat{\boldsymbol{f}} = \frac{\partial F}{\partial \hat{\boldsymbol{\sigma}}} \Rightarrow \boldsymbol{f} = \frac{\hat{\boldsymbol{f}}}{1+\kappa}. \tag{3.6}$$

Proof. From (3.2), we have $\hat{\boldsymbol{f}} = \partial F/\partial \hat{\boldsymbol{\sigma}} = 2\boldsymbol{M} : \hat{\boldsymbol{\xi}}$. From (3.5), we have $\boldsymbol{f} = \partial f/\partial \boldsymbol{\sigma} = 2\boldsymbol{M} : \boldsymbol{\xi} = 2\boldsymbol{M} : (\boldsymbol{\sigma} - \boldsymbol{\alpha}) = 2\boldsymbol{M} : (\hat{\boldsymbol{\sigma}} - \boldsymbol{\beta})/(1+\kappa) = 2\boldsymbol{M} : \hat{\boldsymbol{\xi}}/(1+\kappa)$, which proves (3.6). This result shows that the stress gradient tensor at the stress point $\boldsymbol{\sigma}$ on f has the same direction as the stress gradient tensor at the image stress point $\hat{\boldsymbol{\sigma}}$ on F. □

Although not absolutely essential, it is convenient to assume an 'associative' flow rule with the bounding surface formulation. Here, the term 'associative' implies that the direction of $\dot{\boldsymbol{\epsilon}}^{\mathrm{p}}$ at the current stress point $\boldsymbol{\sigma}$ is given by the gradient $\hat{\boldsymbol{f}}$ at the image stress point $\hat{\boldsymbol{\sigma}}$ [10]. By (3.6) this gradient may be replaced by $\boldsymbol{f}$, and so we can write the constitutive equation as

$$\dot{\boldsymbol{\sigma}} = \boldsymbol{c}^{\mathrm{e}} : (\dot{\boldsymbol{\epsilon}} - \dot{\gamma}\boldsymbol{f}) = \dot{\boldsymbol{\sigma}}^{\mathrm{tr}} - \dot{\gamma}\boldsymbol{c}^{\mathrm{e}} : \boldsymbol{f}. \tag{3.7}$$

The following proposition describes the condition for the continuing evolution of the loading function f.

Proposition 3. *Given a loading function* f *that is homologous to* F, *and an associative flow rule*, $\dot{\boldsymbol{\epsilon}}^{\mathrm{p}} = \dot{\gamma}\boldsymbol{f}$. *If* $\boldsymbol{f} : \boldsymbol{c}^{\mathrm{e}} : \boldsymbol{f} + \mathscr{H} > 0$, *where* $\mathscr{H}$ *is the effective plastic modulus at the current stress point* $\boldsymbol{\sigma}$ *on* f, *then* $\dot{F} = 0$ *implies* $\boldsymbol{f} : \dot{\boldsymbol{\sigma}}^{\mathrm{tr}} > 0$.

Proof. By Proposition 1, $F = \dot{F} = 0$ is equivalent to $f = \dot{f} = 0$. Setting $\dot{f} = 0$ and using (3.7) gives

$$\dot{f} = \boldsymbol{f} : \dot{\boldsymbol{\sigma}}^{\mathrm{tr}} - \dot{\gamma}\underbrace{(\boldsymbol{f} : \boldsymbol{c}^{\mathrm{e}} : \boldsymbol{f} + \mathscr{H})}_{>0} = 0. \tag{3.8}$$

Since $\dot{\gamma} > 0$ for plastic loading, it follows that $\boldsymbol{f} : \dot{\boldsymbol{\sigma}}^{\mathrm{tr}} > 0$. This defines the condition for continuing evolution of the loading function f. Furthermore, since $\boldsymbol{f} : \boldsymbol{c}^{\mathrm{e}} : \boldsymbol{f} > 0$ by the positive-definiteness of $\boldsymbol{c}^{\mathrm{e}}$, then this result also holds in the softening regime (i.e. $\mathscr{H} < 0$) provided that $\mathscr{H} > -\boldsymbol{f} : \boldsymbol{c}^{\mathrm{e}} : \boldsymbol{f}$. □

To summarize, continuing evolution of f requires that $\dot{f} = 0$ and $\boldsymbol{f} : \dot{\boldsymbol{\sigma}}^{\mathrm{tr}} > 0$. Furthermore, (3.8) determines the consistency parameter as

$$\dot{\gamma} = \frac{\boldsymbol{f} : \dot{\boldsymbol{\sigma}}^{\mathrm{tr}}}{\boldsymbol{f} : \boldsymbol{c}^{\mathrm{e}} : \boldsymbol{f} + \mathscr{H}} \tag{3.9}$$

and results in a continuum elastoplastic tangential moduli tensor of the form

$$\boldsymbol{c}^{\mathrm{ep}} = \boldsymbol{c}^{\mathrm{e}} - \frac{1}{\chi}\boldsymbol{c}^{\mathrm{e}} : \boldsymbol{f} \otimes \boldsymbol{f} : \boldsymbol{c}^{\mathrm{e}}, \quad \chi = \boldsymbol{f} : \boldsymbol{c}^{\mathrm{e}} : \boldsymbol{f} + \mathscr{H} > 0. \tag{3.10}$$

Clearly, f very much resembles a yield function; however, $f = 0$ is always true, thus ruling out the possibility that $f < 0$ in the second of the Kuhn–Tucker conditions in $(2.8)_2$, and so f is not a yield function. On the other hand, when $\boldsymbol{f} : \dot{\boldsymbol{\sigma}}^{\mathrm{tr}} < 0$ the theory predicts an instantaneously elastic response, although plasticity ensues immediately thereafter. In this case the old loading function f collapses and a new loading function forms around the current stress point $\boldsymbol{\sigma}$, which now serves as the new homology center. Consequently, the theory effectively assumes a vanishing elastic region [9]. This idea is elaborated further in the next section where a specific example of a bounding surface model based on critical state theory is described.

4. Enhanced Cam-Clay model

In this section we specialize the generalized theory of ellipsoidal yield surfaces described in Section 2 to produce a well-known modified Cam-Clay constitutive theory of critical state soil mechanics. The idea is to use modified Cam-Clay yield surface to represent the bounding surface F, and then enhance it to include plasticity inside this surface using the model described in Section 3.

4.1. Bounding surface model

To obtain more familiar constitutive expressions, it is useful to rewrite (2.1) in the form

$$F = \|\hat{\boldsymbol{s}} - \boldsymbol{\beta}_s\|^2 + c^2(\hat{p} - \beta_p)^2 - c^2(p_{\mathrm{c}} - \beta_p)^2 = 0, \tag{4.1}$$

where

$$\hat{p} = \frac{1}{3}\mathrm{tr}(\hat{\boldsymbol{\sigma}}), \quad \hat{\boldsymbol{s}} = \hat{\boldsymbol{\sigma}} - \hat{p}\boldsymbol{1}, \quad \beta_p = \frac{1}{3}\mathrm{tr}(\boldsymbol{\beta}), \quad \boldsymbol{\beta}_s = \boldsymbol{\beta} - \beta_p\boldsymbol{1} \tag{4.2}$$

and

$$p_{\mathrm{c}} = \beta_p - R/c. \tag{4.3}$$

We identify $p_{\mathrm{c}} < 0$ as the generalized preconsolidation pressure defined in [23,30,31], and represents the most negative root of the quadratic equation (4.1) obtained when we set $\|\hat{\boldsymbol{s}} - \boldsymbol{\beta}_s\|^2 = 0$ (see Fig. 3). The rate form for p_{c} is

$$\dot{p}_{\mathrm{c}} = \dot{\beta}_p - \dot{R}/c. \tag{4.4}$$

Now, let us use a linear combination of isotropic and kinematic hardening to develop a special bounding surface model. For purely isotropic hardening, Eq. (4.4) gives $\dot{\beta}_p = 0$ and $\dot{R} = -c\dot{p}_{\mathrm{c}}$; for purely kinematic hardening, $\dot{R} = 0$ and $\dot{\beta}_p = \dot{p}_{\mathrm{c}}$. Letting the same constant parameter $\zeta \in [0, 1]$, introduced in Section 2, describe the proportions of the two types of hardening, we set

$$\dot{R} = -\zeta c\dot{p}_{\mathrm{c}}, \quad \dot{\beta}_p = (1 - \zeta)\dot{p}_{\mathrm{c}}. \tag{4.5}$$

Clearly, $\zeta = 0$ results in purely kinematic hardening, whereas $\zeta = 1$ results in purely isotropic hardening.

The case $\boldsymbol{\mu} = \boldsymbol{1}/\sqrt{3}$ and $\zeta = 1/2$ is of special interest. Here, the backstress tensor is restricted to move along the hydrostatic axis, while

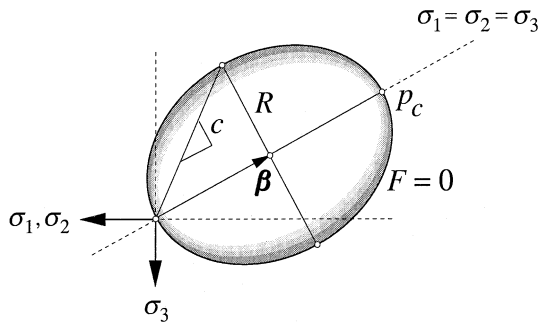

Fig. 3. Modified Cam-Clay ellipsoid.

$$\dot{R} = -c\dot{p}_c/2, \quad \dot{\beta}_p = \dot{p}_c/2. \tag{4.6}$$

To demonstrate the consistency of $(4.6)_2$ with previous developments, let us write the evolution equation for the backstress tensor $\boldsymbol{\beta}$ based on $(2.13)_2$ as

$$\dot{\boldsymbol{\beta}} = \frac{1}{2}\frac{\hat{\boldsymbol{f}} : \dot{\hat{\boldsymbol{\sigma}}}}{\hat{\boldsymbol{f}} : \boldsymbol{\mu}}\boldsymbol{\mu}. \tag{4.7}$$

Since the ellipsoid is centered about the hydrostatic axis, and since the stress path corresponding to isotropic compression is $\dot{\hat{\boldsymbol{\sigma}}} = \sqrt{3}\dot{p}_c\boldsymbol{\mu}$, then $\dot{\boldsymbol{\beta}} = (\sqrt{3}\dot{p}_c/2)\boldsymbol{\mu} = (\dot{p}_c/2)\mathbf{1} \equiv \dot{\beta}_p\mathbf{1}$. This is consistent with the result shown in $(4.6)_2$.

Finally, let us take the initial condition as $R = 0$ and $\boldsymbol{\beta} = \mathbf{0}$ when $p_c = 0$. Then (4.6) predicts that $R = -cp_c/2$ and $\beta_p = p_c/2$, and so the bounding surface F can be written in the invariant form

$$F = \|\hat{\mathbf{s}}\|^2 + c^2\hat{p}(\hat{p} - p_c) = 0. \tag{4.8}$$

In this case, F is now expressible in terms of the first and second stress invariants alone. Eq. (4.8) defines an ellipsoid in principal stress space that is generated by the hydrostatic axis and passes through the origin (see Fig. 3).

4.2. Hardening law

Let us now enhance the model by allowing plastic deformation to take place inside the bounding surface. Recall that this is facilitated by an ellipsoidal loading function of the form

$$f = \boldsymbol{\xi} : \boldsymbol{M} : \boldsymbol{\xi} - r^2 = 0, \quad \boldsymbol{\xi} = \boldsymbol{\sigma} - \boldsymbol{\alpha}, \quad \boldsymbol{\alpha} = \frac{\kappa\boldsymbol{\sigma}_0 + \boldsymbol{\beta}}{1 + \kappa}. \tag{4.9}$$

To completely describe the evolution of f it is necessary to describe the variation of r (or the variation of $\mathscr{H}$) with respect to κ. Previous authors have used exponential mapping laws for this purpose [8–10,25]. However, whatever hardening law is used it must satisfy the requirements that $\mathscr{H}(\kappa = \infty) = \infty$ and $\mathscr{H}(\kappa = 0) = \hat{\mathscr{H}}$; the former implies instantaneous elastic response on unloading, whereas the latter implies a limiting value of $\hat{\mathscr{H}}$ as $\boldsymbol{\sigma}$ approaches its image point $\hat{\boldsymbol{\sigma}}$.

In Section 2 it was assumed that the tangential plastic modulus can be derived from a free energy function, although this function usually is not available in practice and empirical hardening laws are commonly used. A widely used empirical hardening law in critical state soil mechanics is based on a bilogarithmic relationship between the preconsolidation pressure p_c and the specific volume v [36–38], which gives rise to the rate relationship [23,39]

$$\dot{p}_c = -\Theta p_c\dot{\epsilon}_v^p, \quad \Theta = \frac{1}{\widetilde{\lambda} - \widetilde{\kappa}}, \quad \dot{\epsilon}_v^p = \mathrm{tr}(\dot{\boldsymbol{\epsilon}}^p), \quad \dot{\boldsymbol{\epsilon}}^p = \dot{\boldsymbol{\epsilon}} - \dot{\boldsymbol{\epsilon}}^e, \tag{4.10}$$

where $\widetilde{\lambda}$ and $\widetilde{\kappa}$ are experimentally determined compressibility indices defined in [39]. Equivalently, since $R = -cp_c/2$ and $\dot{R} = -c\dot{p}_c/2$, we have

$$\dot{R} = -\Theta R \mathrm{tr}(\dot{\boldsymbol{\epsilon}}^{\mathrm{p}}). \tag{4.11}$$

Similarly, inside the bounding surface a simple hardening law describing the evolution of r may be written as

$$\dot{r} = -\Theta(r + h\kappa^m)\mathrm{tr}(\dot{\boldsymbol{\epsilon}}^{\mathrm{p}}), \tag{4.12}$$

where h and m are additional material parameters describing the degradation of the slope of the stress–strain curve inside F. It is easy to see that (4.12) predicts an initially stiffer response due to the presence of the extra term $h\kappa^m$, but this hardening law approaches (4.11) as $\kappa \to 0$.

4.3. Nonlinear hyperelasticity

A final ingredient of the constitutive model is an energy-conserving elasticity model capable of representing pressure-dependent elastic bulk and shear moduli. To this end, we use a class of two-invariant stored energy functions describing the hyperelastic characteristics of soils. An energy-conserving model provides a fundamentally correct description of elastic material behavior even in the regime of plastic responses.

Following [23,39], we consider a class of stored energy functions of the form

$$\Psi^{\mathrm{e}} = -p_0\widetilde{\kappa}\exp\left(-\frac{\epsilon_v^{\mathrm{e}} - \epsilon_{v0}^{\mathrm{e}}}{\widetilde{\kappa}}\right) + \frac{3}{2}\mu^{\mathrm{e}}(\epsilon_s^{\mathrm{e}})^2, \tag{4.13}$$

where

$$\epsilon_v^{\mathrm{e}} = \mathrm{tr}(\boldsymbol{\epsilon}^{\mathrm{e}}), \quad \epsilon_s^{\mathrm{e}} = \sqrt{\frac{2}{3}}\|\boldsymbol{e}^{\mathrm{e}}\|, \quad \boldsymbol{e}^{\mathrm{e}} = \boldsymbol{\epsilon}^{\mathrm{e}} - \frac{1}{3}\epsilon_v^{\mathrm{e}}\mathbf{1}, \tag{4.14}$$

and $\epsilon_{v0}^{\mathrm{e}}$ is the reference elastic volumetric strain corresponding to a mean normal stress p_0; $\widetilde{\kappa}$ the same compressibility index introduced in (4.10); and μ^{e} is the variable elastic shear modulus defined by the expression

$$\mu^{\mathrm{e}} = \mu_0 - \alpha p_0 \exp\left(-\frac{\epsilon_v^{\mathrm{e}} - \epsilon_{v0}^{\mathrm{e}}}{\widetilde{\kappa}}\right). \tag{4.15}$$

A constant value $\mu_0 > 0$ of shear modulus is obtained by setting the parameter $\alpha = 0$, while a pressure-dependent shear modulus is obtained by setting $\mu_0 = 0$ and $\alpha > 0$. The stored energy function Ψ^{e} may be interpreted as part of the free energy function $\Psi(\boldsymbol{\epsilon}^{\mathrm{e}}, \theta)$ introduced in Section 2.

Details of the nonlinear hyperelastic model described above can be found in [23,39]. For future reference, we adopt their notations and write the elastic rate constitutive equation as

$$\dot{\boldsymbol{\sigma}} = \boldsymbol{c}^{\mathrm{e}} : \dot{\boldsymbol{\epsilon}}^{\mathrm{e}}, \tag{4.16}$$

where $\boldsymbol{c}^{\mathrm{e}}$ is the Hessian tensor defined in (2.14) which takes the explicit form

$$\boldsymbol{c}^{\mathrm{e}} = \frac{2}{3}D_{22}^{\mathrm{e}}\boldsymbol{I} + \left(D_{11}^{\mathrm{e}} - \frac{2}{9}D_{22}^{\mathrm{e}}\right)\mathbf{1}\otimes\mathbf{1} + \sqrt{\frac{2}{3}}D_{12}^{\mathrm{e}}(\mathbf{1}\otimes\hat{\boldsymbol{n}} + \hat{\boldsymbol{n}}\otimes\mathbf{1}), \tag{4.17}$$

where $\hat{\boldsymbol{n}} = \boldsymbol{e}^{\mathrm{e}}/\|\boldsymbol{e}^{\mathrm{e}}\|$, and D_{ij}^{e} are coefficients relating the rates of stress and strain invariants via

$$\begin{Bmatrix} \dot{p} \\ \dot{q} \end{Bmatrix} = \begin{bmatrix} D_{11}^{\mathrm{e}} & D_{12}^{\mathrm{e}} \\ D_{12}^{\mathrm{e}} & D_{22}^{\mathrm{e}} \end{bmatrix} \begin{Bmatrix} \dot{\epsilon}_v^{\mathrm{e}} \\ \dot{\epsilon}_s^{\mathrm{e}} \end{Bmatrix} \tag{4.18}$$

in which $p = \mathrm{tr}(\boldsymbol{\sigma})/3$ and $q = \sqrt{3/2}\|\boldsymbol{s}\|$. The major symmetry of $\boldsymbol{c}^{\mathrm{e}}$ follows directly from the assumed existence of a stored energy function, while its minor symmetry follows from the symmetry of the elastic small

strain tensor. Note that $\boldsymbol{c}^{\mathrm{e}}$ is not always invertible, and a condition for its invertibility is given in [35] in terms of the maximum value attrained by the stress ratio q/p. For practical reasons this maximum stress ratio is not likely to be attained by real soils, and so in this paper it is assumed that the moduli tensor $\boldsymbol{c}^{\mathrm{e}}$ is positive-definite and invertible.

5. Continuum formulation

This section describes the evolution equations in rate form for the bounding surface model, as well as demonstrates the well-posedness of the theory. In particular, cases where $\kappa = 0$ and $\kappa > 0$ are discussed.

5.1. Case 1: $f = F$ and $\kappa = 0$

Here, the bounding and loading functions coincide, and the problem reduces to that discussed in [23]. With $\boldsymbol{\sigma}$ substituted for $\hat{\boldsymbol{\sigma}}$, we have

$$\mathscr{H} = \hat{\mathscr{H}} = -\frac{1}{\dot{\gamma}}\frac{\partial F}{\partial R}\dot{R}, \tag{5.1}$$

where

$$\frac{\partial F}{\partial R} = -2\boldsymbol{\xi} : \boldsymbol{M} : \frac{\partial \boldsymbol{\beta}}{\partial R} - 2R = 2cp \tag{5.2}$$

and

$$\dot{R} = -\dot{\gamma}\Theta R \mathrm{tr}(\boldsymbol{f}), \quad \mathrm{tr}(\boldsymbol{f}) = 2c(R + cp). \tag{5.3}$$

The plastic modulus can now be expressed in the alternative forms

$$\mathscr{H} = 4\Theta c^2 pR(R + cp) = \Theta c^4 p p_{\mathrm{c}}(p_{\mathrm{c}} - 2p). \tag{5.4}$$

The latter form predicts a hardening response ($\mathscr{H} > 0$) when $p < p_{\mathrm{c}}/2 = -R/c$, and a softening response ($\mathscr{H} < 0$) otherwise. As before, the consistency parameter is evaluated from the equation

$$\dot{\gamma} = \frac{\boldsymbol{f} : \dot{\boldsymbol{\sigma}}^{\mathrm{tr}}}{\boldsymbol{f} : \boldsymbol{c}^{\mathrm{e}} : \boldsymbol{f} + \mathscr{H}} \tag{5.5}$$

which describes the evolution of plastic deformation.

5.2. Case 2: $f = F/(1+\kappa)^2$ and $\kappa > 0$

Here, the loading function is completely inscribed in the bounding function in a non-touching fashion. A key result to use in this case is given in Proposition 1, which focuses on the loading function f alone and treats it effectively as a yield function. Similar to (5.1), the plastic modulus can be obtained from the expression

$$\mathscr{H} = -\frac{1}{\dot{\gamma}}\frac{\partial f}{\partial r}\dot{r}, \tag{5.6}$$

where

$$\frac{\partial f}{\partial r} = -2\boldsymbol{\xi} : \boldsymbol{M} : \frac{\partial \boldsymbol{\alpha}}{\partial r} - 2r \tag{5.7}$$

and

$$\dot{r} = -\dot{\gamma}\Theta(r + h\kappa^m)\mathrm{tr}(\boldsymbol{f}), \quad \mathrm{tr}(\boldsymbol{f}) = 2c^2(p - \alpha_p). \tag{5.8}$$

Some extra steps are needed to evaluate the derivative in (5.7). First, let us use the chain rule on $(3.4)_2$ to obtain

$$(1+\kappa)\frac{\partial \boldsymbol{\alpha}}{\partial r} = \kappa \frac{\partial \boldsymbol{\sigma}_0}{\partial r} + (\boldsymbol{\sigma}_0 - \boldsymbol{\alpha})\frac{\partial \kappa}{\partial r} + \frac{\partial \boldsymbol{\beta}}{\partial r}. \tag{5.9}$$

Now, since the projection center $\boldsymbol{\sigma}_0$ itself describes a relative position in the bounding surface and therefore is not stationary due to the continuing plastic deformation, the chosen form for F allows us to write it in the form

$$\boldsymbol{\sigma}_0 = \boldsymbol{\Sigma}_0 R, \quad \boldsymbol{\Sigma}_0 = \boldsymbol{\sigma}_0^*/R_0, \tag{5.10}$$

where $\boldsymbol{\sigma}_0^*$ is the stress state at which the "unloading" condition $\boldsymbol{f} : \dot{\boldsymbol{\sigma}}^{\mathrm{tr}} < 0$ is first detected, signifying collapse of the previous loading function and the creation of a new one, and R_0 is the value of R at this transition point. The normalized stress tensor $\boldsymbol{\Sigma}_0$ may thus be assumed constant, and so

$$\frac{\partial \boldsymbol{\sigma}_0}{\partial r} = \boldsymbol{\Sigma}_0 \frac{\partial R}{\partial r}. \tag{5.11}$$

Furthermore, since $\boldsymbol{\beta} = -(R/c)\mathbf{1}$, we have

$$\frac{\partial \boldsymbol{\beta}}{\partial r} = -\frac{1}{c}\frac{\partial R}{\partial r}\mathbf{1}. \tag{5.12}$$

Next, we consider relationship $(3.5)_2$, which is rewritten herein as

$$R = (1+\kappa)r. \tag{5.13}$$

Implicit differentiation with respect to r yields the relationships

$$\frac{\partial R}{\partial r} = 1+\kappa, \quad \frac{\partial \kappa}{\partial r} = -\frac{1+\kappa}{r}, \quad r \neq 0. \tag{5.14}$$

Substituting these results in (5.9) gives

$$\frac{\partial \boldsymbol{\alpha}}{\partial r} = \frac{1}{r}\boldsymbol{\alpha} - \boldsymbol{\Sigma}_0 - \frac{1}{c}\mathbf{1}, \quad r \neq 0. \tag{5.15}$$

The plastic modulus can now be expressed in the form

$$\mathscr{H} = 2\Theta \mathscr{K} c^2 (p - \alpha_p)(r + h\kappa^m), \tag{5.16}$$

where

$$\mathscr{K} = -2(\boldsymbol{s} - \boldsymbol{\alpha}_s) : \left(\frac{\boldsymbol{\alpha}_s}{r} - \boldsymbol{\Sigma}_0'\right) - 2c^2(p - \alpha_p)\left(\frac{\alpha_p}{r} - P_0 - \frac{1}{c}\right) - 2r \tag{5.17}$$

and where $P_0 = \mathrm{tr}(\boldsymbol{\Sigma}_0)/3$, $\boldsymbol{\Sigma}_0' = \boldsymbol{\Sigma}_0 - P_0\mathbf{1}$, and $r \neq 0$. Having obtained an expression for $\mathscr{H}$ in closed form, we can again use (5.5) to describe the evolution of plastic deformation.

Remark 1. It is interesting to describe the evolution of the image stress point $\hat{\boldsymbol{\sigma}}$ with plastic deformation. Taking the rate form expression of (3.1) gives

$$\dot{\hat{\boldsymbol{\sigma}}} = \dot{\boldsymbol{\sigma}} + \kappa(\dot{\boldsymbol{\sigma}} - \dot{\boldsymbol{\sigma}}_0) + \dot{\kappa}(\boldsymbol{\sigma} - \boldsymbol{\sigma}_0), \tag{5.18}$$

where $\dot{\boldsymbol{\sigma}} = \dot{\boldsymbol{\sigma}}^{\mathrm{tr}} - \ddot{\gamma}\boldsymbol{c}^{\mathrm{e}} : \boldsymbol{f}$ and $\dot{\boldsymbol{\sigma}}_0 = \boldsymbol{\Sigma}_0 \dot{R}$. But $\dot{R}$ must satisfy the rate form version of (5.13) as

$$\dot{R} = (1+\kappa)\dot{r} + \dot{\kappa} r. \tag{5.19}$$

Consequently, using the hardening laws established individually for $\dot{R}$ and $\dot{r}$, we have

$$\dot{\kappa} = \dot{\gamma}\Theta \mathrm{tr}(\boldsymbol{f})\left[(1+\kappa)\frac{r + h\kappa^m}{r} - \frac{R}{r}\right]. \tag{5.20}$$

Thus, the evolution of $\dot{\hat{\boldsymbol{\sigma}}}$ depends on the value of the parameter $\dot{\gamma}$. By Proposition 1 the image stress rate evaluated from (5.18), together with the established expression for $\dot{R}$, identically satisfies the consistency condition $\dot{F} = 0$.

5.3. Case 3: $\boldsymbol{\sigma} = \boldsymbol{\sigma}_0 = \boldsymbol{\alpha}$ and $\kappa \to \infty$

This case corresponds to the instant at which the condition $\boldsymbol{f} : \dot{\boldsymbol{\sigma}}^{\mathrm{tr}} < 0$ is detected, signifying collapse of the previous loading function and the creation of a new one. In this case the loading function is re-centered on the current stress point so that $\boldsymbol{\sigma}_0 = \boldsymbol{\sigma}$ defines the new projection center. Since (3.1) suggests that $\kappa \to \infty$ when $\boldsymbol{\sigma} = \boldsymbol{\sigma}_0$, then $\mathscr{H} \to \infty$ and the response is instantaneously hyperelastic. Thus, the instantaneous constitutive equation on unloading becomes

$$\dot{\boldsymbol{\sigma}} = \boldsymbol{c}^{\mathrm{e}} : \dot{\boldsymbol{\epsilon}} \tag{5.21}$$

where $\boldsymbol{c}^{\mathrm{e}}$ is the Hessian tensor defined in (4.17).

6. Return mapping algorithm in strain space

This section presents a return mapping algorithm for the anisotropic bounding surface model in six-dimensional strain space. A similar return mapping algorithm in two-dimensional strain invariant space was used in [23] for a standard isotropic two-invariant Cam-Clay model. It is shown that extension to the anisotropic case is relatively straightforward, and little modification is needed to make the previous algorithm work for the problem at hand.

6.1. Stress-point integration

We begin by writing the return mapping algorithm as

$$\boldsymbol{\epsilon}^{\mathrm{e}} = \boldsymbol{\epsilon}^{\mathrm{e\,tr}} - \Delta\gamma \boldsymbol{f}, \quad \boldsymbol{\epsilon}^{\mathrm{e\,tr}} = \boldsymbol{\epsilon}^{\mathrm{e}}_n + \Delta\boldsymbol{\epsilon}, \tag{6.1}$$

where $\Delta\gamma > 0$ is the discrete consistency parameter. It is implied in (6.1) that $\boldsymbol{\epsilon}^{\mathrm{e}} = \boldsymbol{\epsilon}^{\mathrm{e}}_{n+1}$, $\boldsymbol{\epsilon}^{\mathrm{e\,tr}} = \boldsymbol{\epsilon}^{\mathrm{e\,tr}}_{n+1}$, and $\boldsymbol{f} = \boldsymbol{f}_{n+1}$ (the subscripts $n+1$ will be omitted throughout this paper to simplify the notations). The algorithm is driven by the trial elastic strain, $\boldsymbol{\epsilon}^{\mathrm{e\,tr}}$, which is obtained by freezing plastic flow. It is assumed that $f(\boldsymbol{\sigma}^{\mathrm{tr}}, r_n) > 0$, where $\boldsymbol{\sigma}^{\mathrm{tr}} = \partial\Psi^{\mathrm{e}}/\partial\boldsymbol{\epsilon}^{\mathrm{e}}$ is the trial elastic stress evaluated at the configuration $\boldsymbol{\epsilon}^{\mathrm{e\,tr}}$, and r_n is the fixed value of r as the plastic flow is frozen. The latter assumption ensures a continuing evolution of the loading function f.

The evolution equation for R from implicit integration of (4.11) is

$$R = \widetilde{R}(\boldsymbol{\epsilon}^{\mathrm{e}}) = \frac{R_n}{1 + \Theta\Delta\epsilon^{\mathrm{p}}_v}, \quad \Delta\epsilon^{\mathrm{p}}_v = \mathrm{tr}(\Delta\boldsymbol{\epsilon}^{\mathrm{p}}) = \mathrm{tr}(\boldsymbol{\epsilon}^{\mathrm{e\,tr}} - \boldsymbol{\epsilon}^{\mathrm{e}}). \tag{6.2}$$

Similarly, implicit integration of (4.12) gives the following evolution equation for r

$$r = \widetilde{r}(\boldsymbol{\epsilon}^{\mathrm{e}}, \kappa) = \frac{r_n - \Theta h\kappa^m \Delta\epsilon^{\mathrm{p}}_v}{1 + \Theta\Delta\epsilon^{\mathrm{p}}_v}. \tag{6.3}$$

Note that exact integration is possible for R but not for r; but since $\dot{R}$ and $\dot{r}$ are related rates, we integrate them using the same implicit technique for numerical consistency.

The homology relation relates r with R through the parameter κ, and takes the form

$$R = (1+\kappa)r. \tag{6.4}$$

Finally, the consistency condition writes

$$f(\boldsymbol{\sigma}, r) = 0. \tag{6.5}$$

Eqs. (6.1)–(6.5) represent simultaneous nonlinear equations in the unknowns $\boldsymbol{\epsilon}^{\mathrm{e}}$, R, r, κ and $\Delta\gamma$.

To elaborate (6.1), we continue by writing out the time-integrated functions f and $\boldsymbol{f}$ as

$$f = \boldsymbol{\xi} : \boldsymbol{M} : \boldsymbol{\xi} - r^2, \quad \boldsymbol{f} = 2\boldsymbol{M} : \boldsymbol{\xi}, \quad \boldsymbol{\xi} = \boldsymbol{\sigma} - \boldsymbol{\alpha}, \quad \boldsymbol{\alpha} = \frac{\kappa\boldsymbol{\Sigma}_0 - \mathbf{1}/c}{1+\kappa} R. \tag{6.6}$$

Implied in (6.6) is that there exists a functional relation between $\boldsymbol{\sigma}$ and $\boldsymbol{\epsilon}^{\mathrm{e}}$ that guarantees an energy-conserving elastic response, as well as captures the pressure-dependence of the elastic bulk and shear moduli common in most soils. These features are provided by the hyperelastic constitutive equation of the form

$$\boldsymbol{\sigma} = \frac{\partial \Psi^{\mathrm{e}}}{\partial \boldsymbol{\epsilon}^{\mathrm{e}}} = \frac{\partial \Psi^{\mathrm{e}}}{\partial \epsilon_v^{\mathrm{e}}} \frac{\partial \epsilon_v^{\mathrm{e}}}{\partial \boldsymbol{\epsilon}^{\mathrm{e}}} + \frac{\partial \Psi^{\mathrm{e}}}{\partial \epsilon_s^{\mathrm{e}}} \frac{\partial \epsilon_s^{\mathrm{e}}}{\partial \boldsymbol{\epsilon}^{\mathrm{e}}} = p\mathbf{1} + \sqrt{\frac{2}{3}} q\boldsymbol{n}, \tag{6.7}$$

where

$$p = \frac{\partial \Psi^{\mathrm{e}}}{\partial \epsilon_v^{\mathrm{e}}} = p_0 \exp \Omega \left[1 + \frac{3\alpha}{2\widetilde{\kappa}} (\epsilon_s^{\mathrm{e}})^2 \right], \quad \Omega = -\frac{\epsilon_v^{\mathrm{e}} - \epsilon_{v0}^{\mathrm{e}}}{\widetilde{\kappa}} \tag{6.8}$$

is the mean normal stress, and

$$q = \frac{\partial \Psi^{\mathrm{e}}}{\partial \epsilon_s^{\mathrm{e}}} = 3(\mu_0^{\mathrm{e}} - \alpha p_0 \exp \Omega)\epsilon_s^{\mathrm{e}} \tag{6.9}$$

is the second invariant of the deviatoric stress tensor. The strain invariants ϵ_v^{e} and ϵ_s^{e} are related to the tensor $\boldsymbol{\epsilon}^{\mathrm{e}}$ through (4.14), while $\boldsymbol{n} = \boldsymbol{e}^{\mathrm{e}}/\|\boldsymbol{e}^{\mathrm{e}}\|$, where $\boldsymbol{e}^{\mathrm{e}} = \boldsymbol{\epsilon}^{\mathrm{e}} - (\epsilon_v^{\mathrm{e}}/3)\mathbf{1}$. The hyperelastic constitutive equation defined above allows an energy-conserving representation of pressure-dependent elastic bulk and shear moduli.

6.2. Linearization

Let $\boldsymbol{b}$ be the generalized residuals and $\boldsymbol{x}$ be the generalized unknowns. Individually, the elements of $\boldsymbol{b}$ and $\boldsymbol{x}$ are

$$\boldsymbol{b} = \begin{Bmatrix} \boldsymbol{b}_1 \\ b_2 \\ b_3 \\ b_4 \\ b_5 \end{Bmatrix} = \begin{Bmatrix} \boldsymbol{\epsilon}^{\mathrm{e}} - \boldsymbol{\epsilon}^{\mathrm{e}\,\mathrm{tr}} + \Delta\gamma \boldsymbol{f} \\ R - \widetilde{R}(\boldsymbol{\epsilon}^{\mathrm{e}}) \\ r - \widetilde{r}(\boldsymbol{\epsilon}^{\mathrm{e}}, \kappa) \\ R - (1+\kappa) r \\ f \end{Bmatrix}, \quad \boldsymbol{x} = \begin{Bmatrix} \boldsymbol{x}_1 \\ x_2 \\ x_3 \\ x_4 \\ x_5 \end{Bmatrix} = \begin{Bmatrix} \boldsymbol{\epsilon}^{\mathrm{e}} \\ R \\ r \\ \kappa \\ \Delta\gamma \end{Bmatrix}. \tag{6.10}$$

The first elements of the arrays $\boldsymbol{b}$ and $\boldsymbol{x}$ are symmetric rank-two tensors, so setting $\boldsymbol{b} = \mathbf{0}$ effectively produces 10 equations in 10 unknowns. The size of the system can be reduced to eight by substituting $\widetilde{R}$ and $\widetilde{r}$ in the homology relation $b_4 = 0$, thus effectively eliminating R and r from the list of unknowns (see Appendix A for an alternative formulation of the simultaneous nonlinear equations in eight unknowns).

Newton's method can now be used to solve the above problem. It consists of iterating over the loop

$$\boldsymbol{x}^{k+1} = \boldsymbol{x}^k + \delta\boldsymbol{x}^k, \quad -\boldsymbol{A}^k \delta\boldsymbol{x}^k = \boldsymbol{b}^k, \quad k \leftarrow k+1, \tag{6.11}$$

where $\boldsymbol{A}^k = \boldsymbol{b}'(\boldsymbol{x}^k)$ is the consistent Jacobian of the residuals which takes the explicit form

$$\boldsymbol{A}^k = \begin{bmatrix} (\boldsymbol{I} + \Delta\gamma\boldsymbol{\phi} : \boldsymbol{c}^{\mathrm{e}}) & -\Delta\gamma\boldsymbol{\phi} : \boldsymbol{\alpha}_{,R} & \mathbf{0} & -\Delta\gamma\boldsymbol{\phi} : \boldsymbol{\alpha}_{,\kappa} & \boldsymbol{f} \\ -\rho\mathbf{1} & 1 & 0 & 0 & 0 \\ -\eta\mathbf{1} & 0 & 1 & v & 0 \\ \mathbf{0} & 1 & -(1+\kappa) & -r & 0 \\ \boldsymbol{f} : \boldsymbol{c}^{\mathrm{e}} & -\boldsymbol{f} : \boldsymbol{\alpha}_{,R} & -2r & -\boldsymbol{f} : \boldsymbol{\alpha}_{,\kappa} & 0 \end{bmatrix}. \tag{6.12}$$

The individual derivatives are given by

$$\boldsymbol{\phi} = \frac{\partial^2 f}{\partial \boldsymbol{\sigma} \partial \boldsymbol{\sigma}} = 2\boldsymbol{M}, \quad \boldsymbol{\alpha}_{,R} = \frac{\partial \boldsymbol{\alpha}}{\partial R} = \frac{\kappa \boldsymbol{\Sigma}_0 - \mathbf{1}/c}{1+\kappa},$$
$$\boldsymbol{\alpha}_{,\kappa} = \frac{\partial \boldsymbol{\alpha}}{\partial \kappa} = \frac{\boldsymbol{\Sigma}_0 + \mathbf{1}/c}{(1+\kappa)^2} R, \quad \rho = \frac{\Theta R}{1 + \Theta \Delta \epsilon_v^{\mathrm{p}}} = \frac{1}{3}\mathrm{tr}\left(\frac{\partial \widetilde{R}}{\partial \boldsymbol{\epsilon}^{\mathrm{e}}}\right), \tag{6.13}$$
$$\eta = \frac{\Theta(h\kappa^m + r)}{1 + \Theta \Delta \epsilon_v^{\mathrm{p}}} = \frac{1}{3}\mathrm{tr}\left(\frac{\partial \widetilde{r}}{\partial \boldsymbol{\epsilon}^{\mathrm{e}}}\right), \quad v = \frac{\Theta m h \kappa^{m-1} \Delta \epsilon_v^{\mathrm{p}}}{1 + \Theta \Delta \epsilon_v^{\mathrm{p}}} = -\frac{\partial \widetilde{r}}{\partial \kappa}.$$

The iteration begins with initial estimates $\boldsymbol{\epsilon}^{\mathrm{e}} = \boldsymbol{\epsilon}^{\mathrm{e\,tr}}$, $R = R_n$, $r = r_n$, $\kappa = \kappa_n$, and $\Delta\gamma = 0$; and is considered to have converged when $\|\boldsymbol{b}\| < \mathrm{TOL}\|\boldsymbol{b}_0\|$, where TOL is some acceptable residual error tolerance and $\boldsymbol{b}_0$ is the initial value of $\boldsymbol{b}$.

6.3. Consistent tangent operator

An advantage of the formulation presented above is that it allows direct evaluation of the algorithmic tangent operator in a manner very similar to that used in conventional plasticity theory. This is a key feature of a robust nonlinear integration algorithm since it is well known that the use of the consistent tangent operator preserves the asymptotic rate of quadratic convergence of the global iterations, and hence leads to optimal efficiency. The consistent tangent operator is obtained from the exact linearization

$$\boldsymbol{c} = \frac{\partial \boldsymbol{\sigma}}{\partial \boldsymbol{\epsilon}^{\mathrm{e\,tr}}} = \frac{\partial \boldsymbol{\sigma}}{\partial \boldsymbol{\epsilon}}. \tag{6.14}$$

Implied in (6.14) is that the differentiation is carried out at each converged configuration derived from the local iteration performed in Section 6.2. Details of the formulation for the consistent tangent operator follow.

Let us take the hyperelastic constitutive relationship $\boldsymbol{\sigma} = \boldsymbol{\sigma}(\boldsymbol{\epsilon}^{\mathrm{e}})$ and differentiate with respect to $\boldsymbol{\epsilon}$ to get

$$\frac{\partial \boldsymbol{\sigma}}{\partial \boldsymbol{\epsilon}} = \frac{\partial \boldsymbol{\sigma}}{\partial \boldsymbol{\epsilon}^{\mathrm{e}}} : \frac{\partial \boldsymbol{\epsilon}^{\mathrm{e}}}{\partial \boldsymbol{\epsilon}} = \boldsymbol{c}^{\mathrm{e}} : \frac{\partial}{\partial \boldsymbol{\epsilon}}(\boldsymbol{\epsilon}^{\mathrm{e\,tr}} - \Delta\gamma \boldsymbol{f}) = \boldsymbol{c}^{\mathrm{e}} : \left[\boldsymbol{I} - \Delta\gamma \boldsymbol{\phi} : \left(\frac{\partial \boldsymbol{\sigma}}{\partial \boldsymbol{\epsilon}} - \frac{\partial \boldsymbol{\alpha}}{\partial \boldsymbol{\epsilon}}\right) - \boldsymbol{f} \otimes \frac{\partial \Delta\gamma}{\partial \boldsymbol{\epsilon}}\right]. \tag{6.15}$$

Since

$$\frac{\partial \boldsymbol{\alpha}}{\partial \boldsymbol{\epsilon}} = \frac{\partial \boldsymbol{\alpha}}{\partial \kappa} \otimes \frac{\partial \kappa}{\partial \boldsymbol{\epsilon}} + \frac{\partial \boldsymbol{\alpha}}{\partial R} \otimes \frac{\partial R}{\partial \boldsymbol{\epsilon}}, \tag{6.16}$$

then (6.15) reduces to

$$(\boldsymbol{c}^{\mathrm{e}-1} + \Delta\gamma \boldsymbol{\phi}) : \frac{\partial \boldsymbol{\sigma}}{\partial \boldsymbol{\epsilon}} - \Delta\gamma \boldsymbol{\phi} : \frac{\partial \boldsymbol{\alpha}}{\partial R} \otimes \frac{\partial R}{\partial \boldsymbol{\epsilon}} - \Delta\gamma \boldsymbol{\phi} : \frac{\partial \boldsymbol{\alpha}}{\partial \kappa} \otimes \frac{\partial \kappa}{\partial \boldsymbol{\epsilon}} + \boldsymbol{f} \otimes \frac{\partial \Delta\gamma}{\partial \boldsymbol{\epsilon}} = \boldsymbol{I}. \tag{6.17}$$

Let us take a similar approach and differentiate R with respect to $\boldsymbol{\epsilon}$ from (6.2) to get

$$(\Delta\gamma\rho\mathbf{1} : \boldsymbol{\phi}) : \frac{\partial \boldsymbol{\sigma}}{\partial \boldsymbol{\epsilon}} + \left(1 - \Delta\gamma\rho\mathbf{1} : \boldsymbol{\phi} : \frac{\partial \boldsymbol{\alpha}}{\partial R}\right)\frac{\partial R}{\partial \boldsymbol{\epsilon}} - \left(\Delta\gamma\rho\mathbf{1} : \boldsymbol{\phi} : \frac{\partial \boldsymbol{\alpha}}{\partial \kappa}\right)\frac{\partial \kappa}{\partial \boldsymbol{\epsilon}} + \rho\mathrm{tr}(\boldsymbol{f})\frac{\partial \Delta\gamma}{\partial \boldsymbol{\epsilon}} = \mathbf{0}. \tag{6.18}$$

Differentiating r from (6.3) yields

$$(\Delta\gamma\eta\mathbf{1} : \boldsymbol{\phi}) : \frac{\partial \boldsymbol{\sigma}}{\partial \boldsymbol{\epsilon}} - \left(\Delta\gamma\eta\mathbf{1} : \boldsymbol{\phi} : \frac{\partial \boldsymbol{\alpha}}{\partial R}\right)\frac{\partial R}{\partial \boldsymbol{\epsilon}} + \frac{\partial r}{\partial \boldsymbol{\epsilon}} + \left(v - \Delta\gamma\eta\mathbf{1} : \boldsymbol{\phi} : \frac{\partial \boldsymbol{\alpha}}{\partial \kappa}\right)\frac{\partial \kappa}{\partial \boldsymbol{\epsilon}} + \eta\mathrm{tr}(\boldsymbol{f})\frac{\partial \Delta\gamma}{\partial \boldsymbol{\epsilon}} = \mathbf{0}. \tag{6.19}$$

Differentiating the homology relation (6.4) gives

$$\frac{\partial R}{\partial \boldsymbol{\epsilon}} - (1+\kappa)\frac{\partial r}{\partial \boldsymbol{\epsilon}} - r\frac{\partial \kappa}{\partial \boldsymbol{\epsilon}} = \mathbf{0}. \tag{6.20}$$

Finally, differentiating the consistency condition (6.5) gives

$$\boldsymbol{f} : \frac{\partial \boldsymbol{\sigma}}{\partial \epsilon} - \left(\boldsymbol{f} : \frac{\partial \boldsymbol{\alpha}}{\partial R} \right) \frac{\partial R}{\partial \epsilon} - 2r \frac{\partial r}{\partial \epsilon} - \left(\boldsymbol{f} : \frac{\partial \boldsymbol{\alpha}}{\partial \kappa} \right) \frac{\partial \kappa}{\partial \epsilon} = \boldsymbol{0}. \tag{6.21}$$

The consistent tangent operator can be obtained from the simultaneous equations (6.17)–(6.21) by performing a static condensation. First, let us re-define scalar variables

$$q_1 = R, \quad q_2 = r, \quad q_3 = \kappa, \quad q_4 = \Delta\gamma. \tag{6.22}$$

Next, define the following second-order tensors

$$\boldsymbol{L}_1 = \Delta\gamma\rho \boldsymbol{1} : \boldsymbol{\phi}, \quad \boldsymbol{L}_2 = \Delta\gamma\eta \boldsymbol{1} : \boldsymbol{\phi}, \quad \boldsymbol{L}_3 = \boldsymbol{0}, \quad \boldsymbol{L}_4 = \boldsymbol{f}. \tag{6.23}$$

Finally, define the following non-singular array

$$[Q_{ij}] = \begin{bmatrix} (1 - \Delta\gamma\rho \boldsymbol{1} : \boldsymbol{\phi} : \boldsymbol{\alpha}_{,R}) & 0 & -(\Delta\gamma\rho \boldsymbol{1} : \boldsymbol{\phi} : \boldsymbol{\alpha}_{,\kappa}) & \rho \mathrm{tr}(\boldsymbol{f}) \\ -(\Delta\gamma\eta \boldsymbol{1} : \boldsymbol{\phi} : \boldsymbol{\alpha}_{,R}) & 1 & (v - \Delta\gamma\eta \boldsymbol{1} : \boldsymbol{\phi} : \boldsymbol{\alpha}_{,\kappa}) & \eta \mathrm{tr}(\boldsymbol{f}) \\ 1 & -(1+\kappa) & -r & 0 \\ -(\boldsymbol{f} : \boldsymbol{\alpha}_{,R}) & -2r & -(\boldsymbol{f} : \boldsymbol{\alpha}_{,\kappa}) & 0 \end{bmatrix}. \tag{6.24}$$

Eqs. (6.18)–(6.21) can then be written in the more compact form

$$\boldsymbol{L}_i : \frac{\partial \boldsymbol{\sigma}}{\partial \epsilon} + \sum_{j=1}^{4} Q_{ij} \frac{\partial q_j}{\partial \epsilon} = \boldsymbol{0}, \quad i = 1, \ldots, 4 \tag{6.25}$$

from which we obtain

$$\frac{\partial q_i}{\partial \epsilon} = -\sum_{j=1}^{4} Q_{ij}^{-1} \boldsymbol{L}_j : \frac{\partial \boldsymbol{\sigma}}{\partial \epsilon}, \quad i = 1, \ldots, 4. \tag{6.26}$$

Now, define second-order tensors

$$\boldsymbol{U}_1 = -\Delta\gamma \boldsymbol{\phi} : \frac{\partial \boldsymbol{\alpha}}{\partial R}, \quad \boldsymbol{U}_2 = \boldsymbol{0}, \quad \boldsymbol{U}_3 = -\Delta\gamma \boldsymbol{\phi} : \frac{\partial \boldsymbol{\alpha}}{\partial \kappa}, \quad \boldsymbol{U}_4 = \boldsymbol{f}. \tag{6.27}$$

Eq. (6.17) rewrites

$$(\boldsymbol{c}^{\mathrm{e}-1} + \Delta\gamma \boldsymbol{\phi}) : \frac{\partial \boldsymbol{\sigma}}{\partial \epsilon} + \sum_{i=1}^{4} \boldsymbol{U}_i \otimes \frac{\partial q_i}{\partial \epsilon} = \boldsymbol{I}. \tag{6.28}$$

Substituting (6.26) in (6.28) and inverting gives the consistent tangent operator

$$\frac{\partial \boldsymbol{\sigma}}{\partial \epsilon} = \left(\boldsymbol{d}^{\mathrm{e}} + \Delta\gamma \boldsymbol{\phi} - \sum_{i=1}^{4} \sum_{j=1}^{4} Q_{ij}^{-1} \boldsymbol{U}_i \otimes \boldsymbol{L}_j \right)^{-1}, \tag{6.29}$$

where $\boldsymbol{d}^{\mathrm{e}} = \boldsymbol{c}^{\mathrm{e}-1}$ is the tangential elastic compliance tensor (see Appendix B). From the implementational standpoint, construction of the consistent tangent operator for the anisotropic bounding surface plasticity model in 3D requires an inversion of a 4×4 matrix and an inversion of a 6×6 matrix. Note that the inversion of $\boldsymbol{c}^{\mathrm{e}}$ can be obtained in closed form, as shown in Appendix B. Thus, the total computational effort is about the same as that required to evaluate the consistent tangent operator for a conventional anisotropic elastoplastic constitutive model, see e.g. [17].

6.4. Unloading condition and hyperelastic response

The discrete counterpart of the condition for unloading described in Section 5.3, $\boldsymbol{f} : \dot{\boldsymbol{\sigma}}^{\mathrm{tr}} < 0$, is

$$f^{\mathrm{tr}} := \boldsymbol{\xi}^{\mathrm{tr}} : \boldsymbol{M} : \boldsymbol{\xi}^{\mathrm{tr}} - r_n^2 < 0, \tag{6.30}$$

where

$$\boldsymbol{\xi}^{\mathrm{tr}} = \boldsymbol{\sigma}^{\mathrm{tr}} - \boldsymbol{\alpha}_n, \quad \boldsymbol{\alpha}_n = \frac{\kappa_n \boldsymbol{\Sigma}_0 - \mathbf{1}/c}{1+\kappa_n} R_n \tag{6.31}$$

and

$$\boldsymbol{\sigma}^{\mathrm{tr}} = \frac{\partial \Psi^{\mathrm{e}}}{\partial \boldsymbol{\epsilon}^{\mathrm{e\,tr}}}, \quad \boldsymbol{\epsilon}^{\mathrm{e\,tr}} = \boldsymbol{\epsilon}^{\mathrm{e}}_n + \Delta\boldsymbol{\epsilon} \tag{6.32}$$

in which the subscript n pertains to the current converged value at the beginning of the load step. As in classical plasticity formulation, the trial loading function f^{tr} is evaluated by freezing plastic flow. Satisfaction of the unloading condition (6.30) results in the collapse of the current loading function leading to an instantaneously hyperelastic response. The new loading function now has a normalized projection center at $\boldsymbol{\Sigma}^*_0 = \boldsymbol{\sigma}_n/R_n$ and a characteristic size of $r^*_n = 0$ at the beginning of the current unloading step.

While in principle plasticity is expected to develop right at the onset of unloading, in practice the magnitude of plastic deformation may be too small initially that it normally takes a finite value of r to develop for plastic deformation to be numerically significant. This motivates the introduction of an 'elastic nucleus' representing the smallest loading function within which the response may be taken as purely hyperelastic. Inside the elastic nucleus the update equation for the Cauchy stress tensor takes the form

$$\boldsymbol{\sigma} = \frac{\partial \Psi^{\mathrm{e}}}{\partial \boldsymbol{\epsilon}^{\mathrm{e}}}, \quad \boldsymbol{\epsilon}^{\mathrm{e}} = \boldsymbol{\epsilon}^{\mathrm{e}}_n + \Delta\boldsymbol{\epsilon} \tag{6.33}$$

while the consistent tangent operator takes the form

$$\frac{\partial \boldsymbol{\sigma}}{\partial \boldsymbol{\epsilon}} = \frac{\partial^2 \Psi^{\mathrm{e}}}{\partial \boldsymbol{\epsilon}^{\mathrm{e}} \partial \boldsymbol{\epsilon}^{\mathrm{e}}} = \boldsymbol{c}^{\mathrm{e}}, \tag{6.34}$$

where $\boldsymbol{c}^{\mathrm{e}}$ is defined in (4.17).

With the notion of a finite elastic nucleus in place, we now turn to its precise mathematical description as follows. Let $\boldsymbol{\Sigma}^*_0$ describe the new normalized projection center so that $\boldsymbol{\sigma}^*_0 = \boldsymbol{\Sigma}^*_0 R$, and $\boldsymbol{\sigma}$ denote the current stress point. By definition, the loading function f that passes through $\boldsymbol{\sigma}$ and has this new projection center must remain homologous to F. By radial mapping, we have

$$F = \hat{\boldsymbol{\sigma}} : \boldsymbol{M} : \hat{\boldsymbol{\sigma}} - R^2 = 0, \quad \hat{\boldsymbol{\sigma}} = \boldsymbol{\sigma} + \kappa(\boldsymbol{\sigma} - \boldsymbol{\sigma}_0) \tag{6.35}$$

from which we obtain a quadratic equation for κ:

$$a\kappa^2 + b\kappa + c = 0 \Rightarrow \kappa = \frac{-b + \sqrt{b^2 - 4ac}}{2a}, \tag{6.36}$$

where

$$a := (\boldsymbol{\sigma} - \boldsymbol{\sigma}^*_0) : \boldsymbol{M} : (\boldsymbol{\sigma} - \boldsymbol{\sigma}^*_0) > 0, \tag{6.37a}$$

$$b := 2(\boldsymbol{\sigma} - \boldsymbol{\sigma}^*_0) : \boldsymbol{M} : (\boldsymbol{\sigma} - \boldsymbol{\beta}), \tag{6.37b}$$

$$c := (\boldsymbol{\sigma} - \boldsymbol{\beta}) : \boldsymbol{M} : (\boldsymbol{\sigma} - \boldsymbol{\beta}) - R^2 < 0. \tag{6.37c}$$

The obvious inequalities in (6.37a) and (6.37c), as well as the requirement that $\kappa \geqslant 0$, justify the selection of the positive sign in the square root. The associated size of the loading function is then given by $r = R/(1+\kappa)$. Now, if r_{c} denotes the characteristic size of the elastic nucleus, then the condition for a continuing hyperelastic response is $r < r_{\mathrm{c}}$.

Remark 2. While in principle r_{c} may be made as small as possible, a numerically stiff algorithm may result for very small values of r_{c}/R, leading to non-convergent *local* iterations. Parametric studies suggest that $r_{\mathrm{c}}/R = 0.10$ leads to optimal balance between accuracy and stability, which means that plastic deformations

are numerically insignificant below this value while the local iterations remain generally convergent. This issue concerning the choice of the size of the elastic nucleus is elaborated further in the numerical examples that follow.

7. Numerical examples

This section assesses the accuracy of the proposed integration algorithm and solves a boundary-value problem illustrating the significance of plastic deformation inside the bounding surface on the quasi-static response of a strip footing.

7.1. Isotropic compression

The first problem of interest involves isotropic loading from an initial isotropic stress state. For convenience in presentation, we sketch stress paths on the p,q-plane, where $p = \mathrm{tr}(\boldsymbol{\sigma})/3$ and $q = \sqrt{3/2}\|\boldsymbol{s}\|$. The initial stress point is defined by $\sigma_{11} = \sigma_{22} = \sigma_{33} = -100$ kPa, with all shear stress components being zero, see point A in Fig. 4. Taking a reference value of $\epsilon^{\mathrm{e}}_{v0} = 0$ and assuming $\boldsymbol{\epsilon}^{\mathrm{e}} = \mathbf{0}$ initially, a reference pressure of $p_0 = -100$ kPa ensures that the parameters of the hyperelastic model are consistent with the given initial stress condition. Assuming further that $\boldsymbol{\Sigma}_0 = \mathbf{0}$ initially, we obtain a projection center that coincides with the stress space origin. The loading surface has $r = 50$ kPa while the bounding surface has $R = 75$ kPa initially. In the language of soil mechanics, the soil is slightly overconsolidated with an initial overconsolidation ratio of $\mathrm{OCR} = 75/50 = 1.5$.

The remaining parameters of the model are assumed as follows: ellipsoidal axis ratio $c = 1.0$; hyperelastic compressibility parameter $\widetilde{\kappa} = 0.018$; elastic shear modulus $\mu_0 = 5.4$ MPa; hyperelastic parameter $\widetilde{\alpha} = 0$; compressibility parameter $\widetilde{\lambda} = 0.13$; hardening parameter $h = 5.0$ MPa; and hardening parameter $m = 1.5$. The value of $\widetilde{\alpha} = 0$ uncouples the elastic volumetric and deviatoric responses and leads to a constant elastic shear modulus having a value of μ_0; the elastic bulk modulus remains proportional to the mean normal stress.

Consider now an imposed isotropic compression in which $\Delta\epsilon_{11} = \Delta\epsilon_{22} = \Delta\epsilon_{33} = -0.01$ so that $\Delta\epsilon_v = -0.03$. Fig. 5 compares the mean normal stress responses of the stress point obtained by applying the strain increment in 10 and 100 subincrements. As shown in Fig. 5, the 10-step solution is practically the same as the 100-step solution for plotting purposes. The same can be said of the variations of r and R during isotropic compression, as shown in Fig. 6. It must be noted from Fig. 6 that r approaches R asymptotically, but never equals it, unless the initial condition is such that $r = R$. This is an important feature of the proposed stress-point integration algorithm since it rules out the possibility that r could exceed R during the course of the iteration for a given load increment, leading to a simple but robust algorithm.

For comparison purposes Figs. 5 and 6 also show the 100-step solution obtained by setting $h = 500$ MPa, 100 times larger than the previous value, forcing the model to behave in a nearly elastic fashion inside the

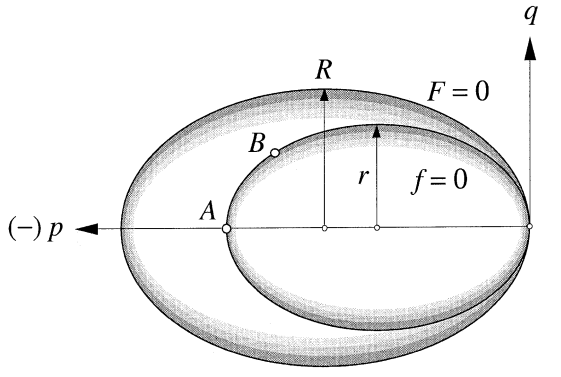

Fig. 4. Accuracy and convergence analyses: initial stress points A and B on p,q-plane.

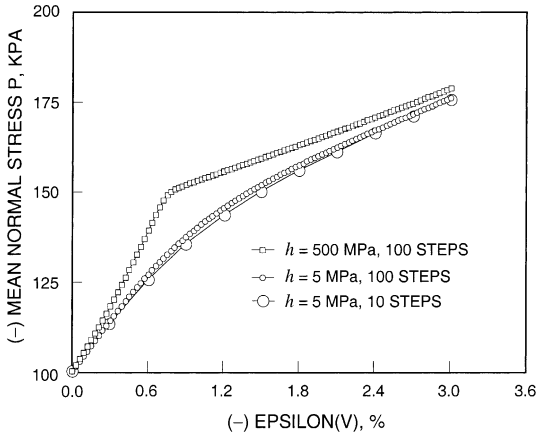

Fig. 5. Accuracy analysis: variation of mean normal stress with volumetric strain for isotropic compression example.

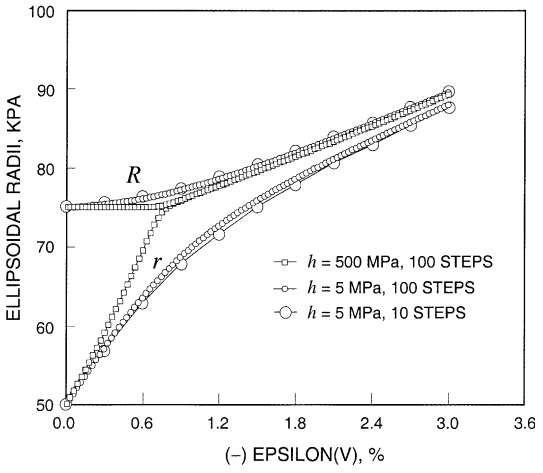

Fig. 6. Accuracy analysis: variation of ellipsoidal radii with volumetric strain for isotropic compression example.

bounding surface. Thus we capture a response predicted by the standard elastoplastic modified Cam-Clay model described in [23]. As evident in Fig. 5 the mean normal stress–volumetric strain response curve is initially concave upward in the elastic regime due to the accompanying increase in the elastic bulk modulus with isotropic confining pressure. During the nearly elastic loading phase the radial parameter R remains approximately constant in the absence of significant plastic deformation (Fig. 6). The concave upward behavior during the elastic loading phase shown in Fig. 5 is not a typical clay response and well illustrates a drawback of standard Cam-Clay theory that is corrected by the proposed bounding surface formulation.

7.2. Simple shearing

Starting from the same initial point A shown in Fig. 4 we now subject the stress point to simple shearing by applying $\Delta\gamma_{12} = 0.05$ in 10 and 100 subincrements, with all other strain increments equal to zero. This results in shearing at a constant volume. Figs. 7 and 8 show variations of the shear stress and ellipsoidal radii r and R during the course of shearing. Again, note that r only approaches R asymptotically but does not equal it. For comparison purposes the 100-step solution for the case $h = 500$ MPa is again compared with the 100-step solution for the case $h = 5$ MPa in both figures. Note that the shear stress varies approximately linearly with shear strain inside the bounding surface for the case $h = 500$ MPa, a consequence of a constant elastic shear modulus assumption that does not necessarily represent a typical clay response.

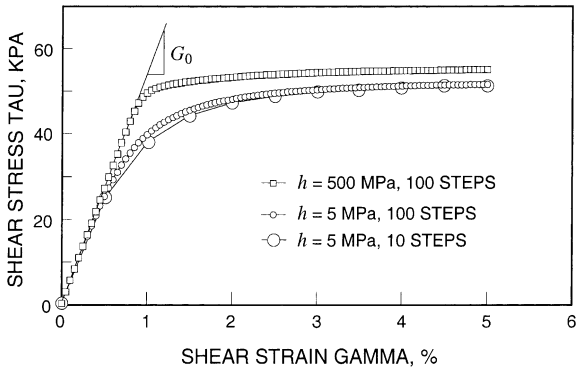

Fig. 7. Accuracy analysis: variation of shear stress with shear strain for simple shearing example.

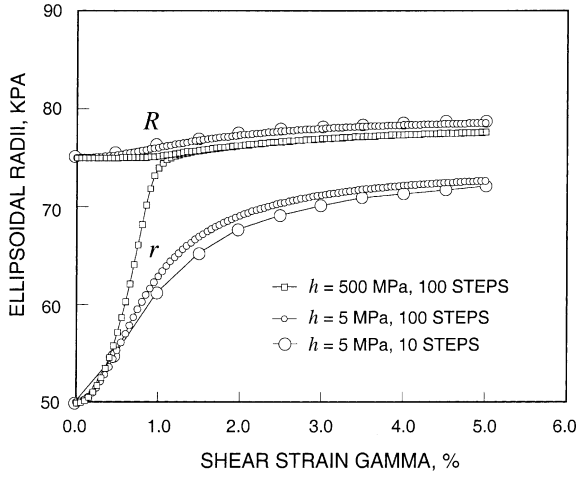

Fig. 8. Accuracy analysis: variation of ellipsoidal radii with shear strain for simple shearing example.

This feature, that no plastic deformation is possible unless the yield surface is reached, well illustrates another drawback of the standard elastoplastic modified Cam-Clay model that is corrected by the proposed bounding surface formulation.

Fig. 9 compares the stress paths resulting from simple shearing for $h = 5$ MPa and $h = 500$ MPa cases. Both stress paths approach the critical state line, CSL, where shearing is possible without plastic volume change [28]. Note that the stress path curves to the right even well inside the bounding surface for the case $h = 5$ MPa, but remains nearly vertical for the case $h = 500$ MPa, until it is sufficiently near the bounding surface. A vertical stress path is a characteristic feature of the nonlinear hyperelastic model with a constant elastic shear modulus and indicates uncoupled volumetric–deviatoric responses in the elastic regime [35].

7.3. Isoerror maps

In order to further assess the accuracy of the proposed integration algorithm, isoerror maps are used in the manner described in [18]. Here, we define a relative error introduced by the numerical integration algorithm from the expression

$$\mathrm{ERR} = \frac{\sqrt{(\boldsymbol{\sigma} - \boldsymbol{\sigma}^*) : (\boldsymbol{\sigma} - \boldsymbol{\sigma}^*)}}{\sqrt{\boldsymbol{\sigma}^* : \boldsymbol{\sigma}^*}} \times 100\%, \tag{7.1}$$

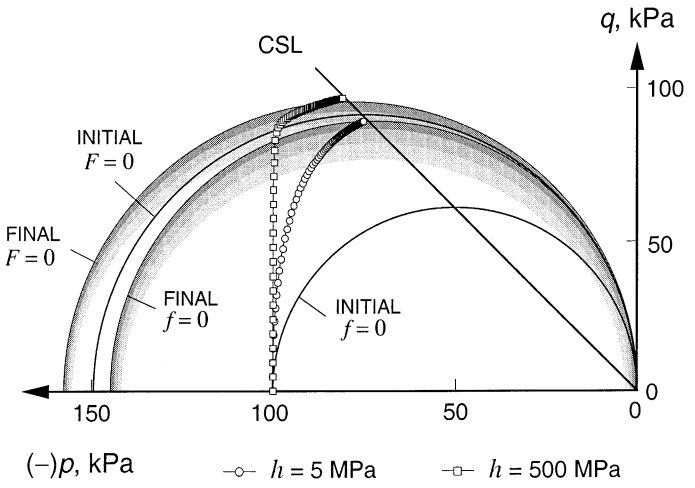

Fig. 9. Stress path on p, q-plane for simple shearing example. Note: Final bounding and loading surfaces correspond to $h = 5$ MPa case.

where $\boldsymbol{\sigma}$ is the result obtained by applying the algorithm, whereas $\boldsymbol{\sigma}^*$ is the exact solution corresponding to the specified strain increment. The exact solution for any given strain increment is obtained by repeatedly applying the algorithm with increasing number of subincrements. The value for which further subincrementation produces no significant change in the numerical results is taken as the exact solution. A preliminary assessment of the order of convergence of the algorithm showed that an analysis performed with 1000 strain subincrements results in solutions that are accurate enough to be considered 'exact'.

The values of material parameters used for generating isoerror maps are the same as those reported in Section 7.1 except that the parameter h was reduced to 1 MPa to further magnify the effects of plastic deformation inside the bounding surface. Four isoerror maps are generated corresponding to permutations from two initial stress conditions and two initial overconsolidation ratios. Initial stress condition A has $\sigma_{11} = \sigma_{22} = \sigma_{33} = -100$ kPa on the isotropic line p as shown in Fig. 4; initial stress condition B lies on the same ellipsoid containing point A as shown in Fig. 4, but with $|q/p| = 0.70$ on the compactive side of the loading surface. Both initial stress conditions were combined with initial overconsolidation ratios of 1.0 and 1.5, where the respective ellipsoidal radii are $r = R = 50$ kPa for the OCR $= 1$ case, and $r = 2R/3 = 50$ kPa for the OCR $= 1.5$ case.

Isoerror maps for loading from initial stress conditions A and B are generated by applying linear combinations of isotropic compression and deviatoric shearing. For purposes of definition, isotropic compression entails applying equal compressive strain increments $\Delta\epsilon_{11} = \Delta\epsilon_{22} = \Delta\epsilon_{33} < 0$ while holding all shear strain increments to zero; deviatoric shearing entails applying equal shear strain increments $\Delta\gamma_{11} = \Delta\gamma_{22} = \Delta\gamma_{33}$ while holding all normal strain increments to zero. Isoerror maps are then plotted on a plane defined by the volumetric step size (VSS) and deviatoric step size (DSS) axes, where $\text{VSS} = \Delta\epsilon_{11} + \Delta\epsilon_{22} + \Delta\epsilon_{33}$, and $\text{DSS} = \sqrt{(\Delta\gamma_{12}^2 + \Delta\gamma_{23}^2 + \Delta\gamma_{13}^2)/3}$.

Isoerror maps for loading from initial stress condition A are shown in Fig. 10(a) for the OCR $= 1.0$ case, and in Fig. 10(b) for the OCR $= 1.5$ case. In Fig. 10(a) the initial loading and bounding surfaces are coincident, and remain coincident throughout the loading process. Thus, this case reduces to the standard elastoplastic critical state model presented in [23]. Note that errors generally increase with increasing step size in both isotropic compression and deviatoric shearing directions. On the other hand, isoerror maps for the OCR $= 1.5$ case shown in Fig. 10(b) slightly increase with isotropic compression, and then decrease beyond the point where the loading and bounding surfaces are nearly coincident. In general, errors are smaller for the initially overconsolidated case because plastic deformations are correspondingly smaller.

Isoerror maps for loading from initial stress condition B are shown in Fig. 11(a) for the OCR $= 1.0$ case, and in Fig. 11(b) for the OCR $= 1.5$ case. Compared to Fig. 10 where errors for the isotropic case are smaller toward the hydrostatic region where the stress ratio is $|q/p| = 0$, errors for the anisotropic case are seen to be smaller toward a region where $|q/p| \neq 0$. Isoerror maps clearly depend on the initial stress state

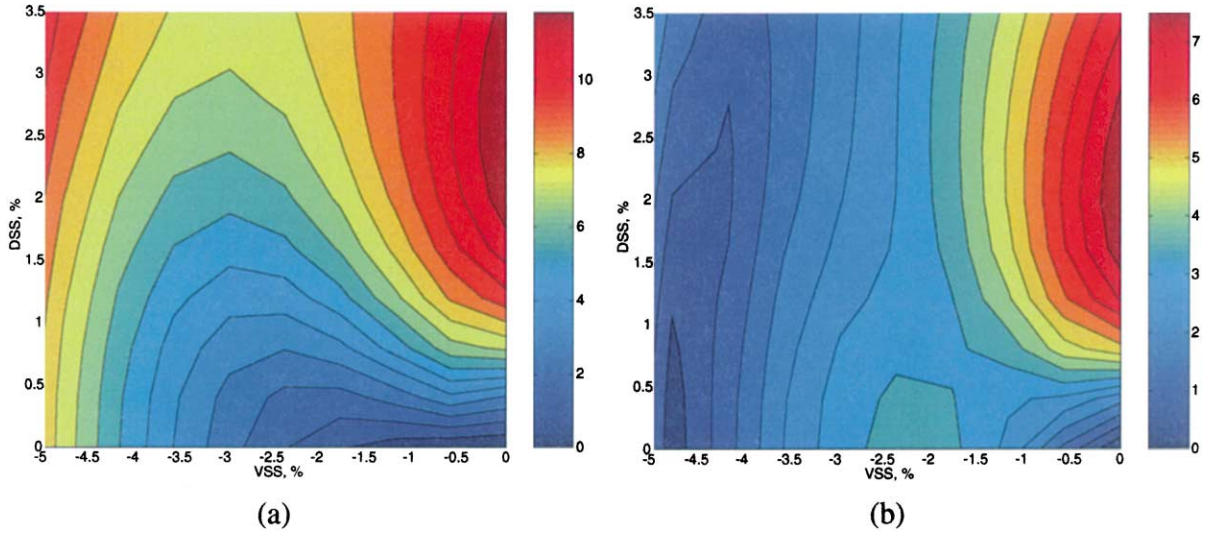

Fig. 10. Isoerror map for loading from initial isotropic state A: (a) OCR = 1.0; (b) OCR = 1.5.

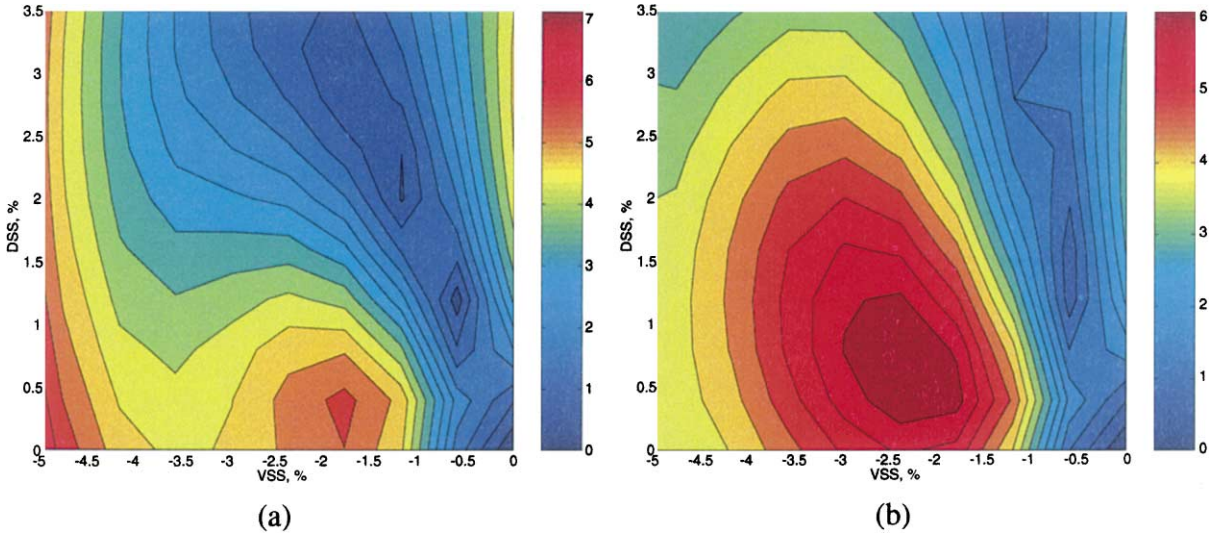

Fig. 11. Isoerror map for loading from initial anisotropic state B: (a) OCR = 1.0; (b) OCR = 1.5.

as well as on the initial overconsolidation ratio. The next examples show how the accuracy of the algorithm may be assessed for the more complicated stress paths involving cyclic loading.

7.4. Strain-controlled cyclic simple shearing

Starting from the same initial condition described in Section 7.1, and assuming this time that $r = R = 50$ kPa initially, we now subject the stress point to cyclic simple shearing consisting of the application of strain increment $\Delta\gamma_{12} = \pm 0.8\%$ applied in 90 and 900 load steps, while holding all other strain increments to zero. Thus, the stress point is forced to shear at a constant volume. Before proceeding to the cyclic stress–strain response, it is useful to illustrate the stress path for this loading condition on the p, q-plane, as shown in Fig. 12. With $f = F$ initially, the stress point is forced to remain on $f = F = 0$ until it is

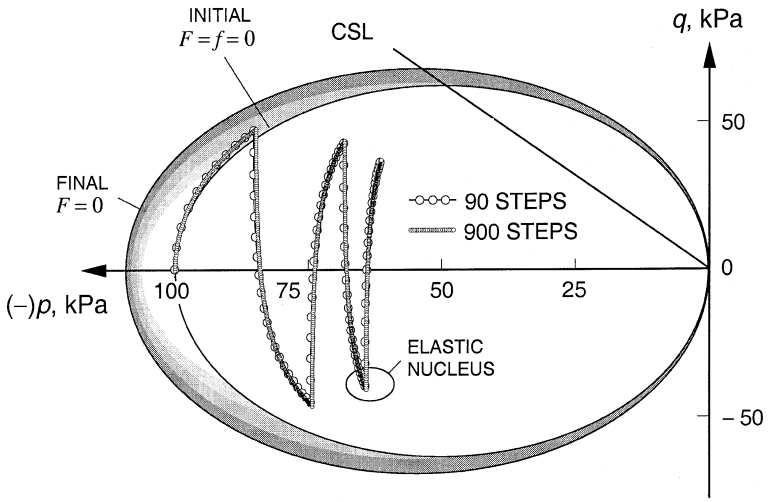

Fig. 12. Stress path on (p, q)-plane for strain-controlled cyclic simple shearing ($h = 5$ MPa case).

first unloaded. The loading function is then re-centered at the first unloading point, where the response is instantaneously elastic and therefore the stress path is instantaneously vertical on the p, q-plane. Observe that the second unloading occurs at a point with a lower absolute value of q (the parameter q carries the sign of the imposed strain increment $\Delta\gamma_{12}$), implying a degradation of shear strength with cyclic loading. This last point is corroborated by the accompanying cyclic stress–strain curve shown in Fig. 13. After two complete cycles the 90-step solution appears to maintain good accuracy relative to the 900-step solution.

Fig. 12 also shows the size of the elastic nucleus with $r_c/R = 0.10$. Note that r_c is defined relative to R, where the latter continues to increase as the bounding surface expands due to continued plastic volumetric compaction predicted inside this surface. The value of $r_c/R = 0.10$ is the optimal ratio alluded to in Remark 2 that leads to a balance between accuracy and stability. To elaborate this point further, Table 1 summarizes the final values of p, q, r, and R as functions of the assumed value of the radial ratio r_c/R at the

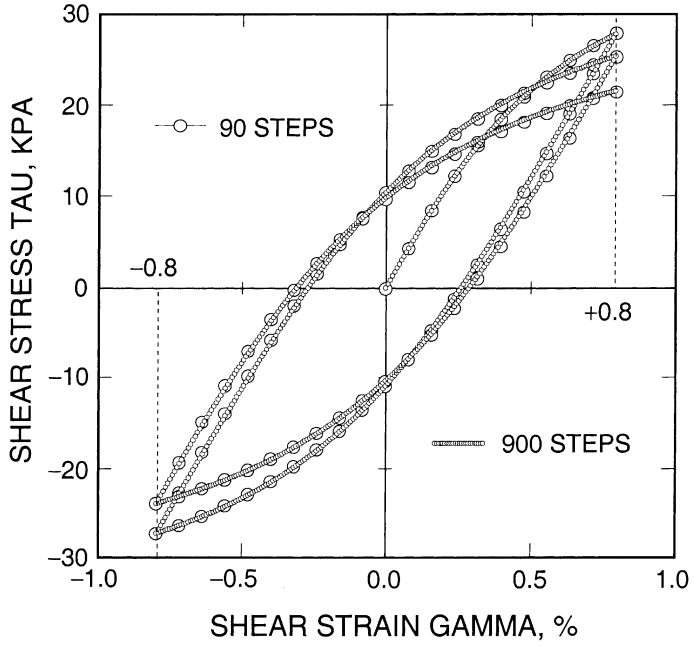

Fig. 13. Shear stress–shear strain curve for strain-controlled cyclic simple shearing ($h = 5$ MPa).

Table 1
Final values of p, q, r and R as functions of r_c/R from 900-step, strain-controlled cyclic simple shearing example (all values in kPa)

r_c/R	$-p$	q	r	R
0.50	61.581	39.594	41.004	54.052
0.20	61.420	37.206	39.576	54.075
0.10	61.413	37.044	39.478	54.076
0.05	61.412	37.016	39.461	54.076
0.01	61.411	37.009	39.457	54.076
0.005	Diverged	Diverged	Diverged	Diverged

conclusion of the 900-step solution. Note that the final values are nearly the same in all cases except when $r_c/R > 0.20$, which affirms the statement that plastic deformation is numerically insignificant when the stress point $\boldsymbol{\sigma}$ is near the projection center $\boldsymbol{\sigma}_0$. However, using very small values of r_c/R results in non-convergent iterations due to numerical ill-conditioning. The value $r_c/R = 0.10$ appears to circumvent this problem not only in this strain-controlled example but also in the stress-controlled problem discussed in the next section.

7.5. Stress-controlled cyclic simple shearing

Stress-controlled cyclic simple shearing requires the solution of an inverse problem $\boldsymbol{\epsilon} = \boldsymbol{\epsilon}(\boldsymbol{\sigma})$ subject to the constraint $\mathrm{tr}(\boldsymbol{\epsilon}) = 0$. Within the context of the bounding surface model, the volume constraint can be imposed by penalization through a constitutive equation of the form

$$\widetilde{\boldsymbol{\sigma}} = \boldsymbol{\sigma}(\boldsymbol{\epsilon}) + \lambda \mathrm{tr}(\boldsymbol{\epsilon})\mathbf{1}, \tag{7.2}$$

where $\lambda \gg 0$ is a penalty parameter. Prescribing a large λ thus forces the satisfaction of the condition $\mathrm{tr}(\boldsymbol{\epsilon}) \to 0$. From a soil mechanics standpoint, λ has the physical significance of being the bulk modulus of water that fully occupies the soil voids, while $-\lambda \mathrm{tr}(\boldsymbol{\epsilon})$ is the pore water pressure generated during undrained shearing [40]. Inhibiting the fluid to move into or out from the soil voids thus forces the saturated soil mass to deform at a constant volume.

Using the functional form (7.2) for the constitutive equation, a stress-controlled problem can be stated as follows: given the evolution of the total stresses $\boldsymbol{\sigma}^*(t)$, find the evolution of the strains $\boldsymbol{\epsilon}^*(t)$ such that (7.2) is satisfied. Now, since (7.2) is a nonlinear functional the solution of the inverse problem requires an iterative strategy. Defining

$$\boldsymbol{r} = \boldsymbol{\sigma}^* - \widetilde{\boldsymbol{\sigma}}, \quad -\boldsymbol{r}'(\boldsymbol{\epsilon}) = \frac{\partial \boldsymbol{\sigma}}{\partial \boldsymbol{\epsilon}} + \lambda \mathbf{1} \otimes \mathbf{1}, \tag{7.3}$$

we can now proceed with Newton iteration to solve the inverse problem.

Starting from the same initial condition described in Section 7.4, we now subject the stress point to volume-conserving cyclic simple shearing ($\lambda = 10^8$ MPa) consisting of the application of stress increment $\sigma^*_{12} = \pm 24$ kPa in 90 and 900 uniform subincrements. Fig. 14 shows that the stress path generated by this imposed cyclic loading resembles that of Fig. 12 except that the stress amplitudes are constant. Fig. 15 portrays the resulting cyclic shear stress–shear strain curve showing amplification of the shear strain with increasing number of cyclic loadings, a feature equivalent to that of shear strain degradation for the case of the strain-controlled behavior depicted in Fig. 13. However, in contrast to the strain-controlled example where the stress integration algorithm retains its overall accuracy, the 90-step solution slightly deviates from the 900-step solution during the latter stage of loading as the strain values continue to amplify.

The performance of the iterative solution is demonstrated in Table 2, which shows the residual norms corresponding to the final load increment, denoted by line AB in Fig. 15, of the 90-step solution. Here, the global iteration number pertains to the solution of the stress-controlled problem, Eq. (7.3), and so for the 90-step solution the initial norm of the residual vector is equal to $24/10 = 2.4$ kPa. Each global iteration requires an iterative solution of the local problem. For purposes of presentation the convergence profiles of

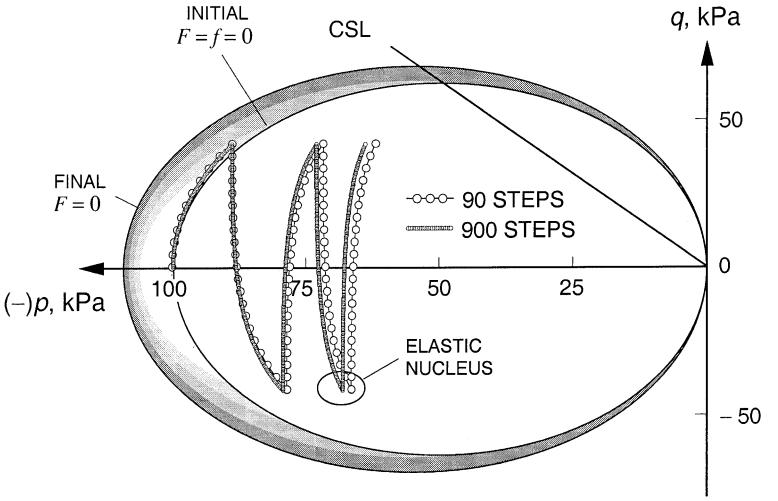

Fig. 14. Stress path on (p, q)-plane for stress-controlled cyclic simple shearing ($h = 5$ MPa case).

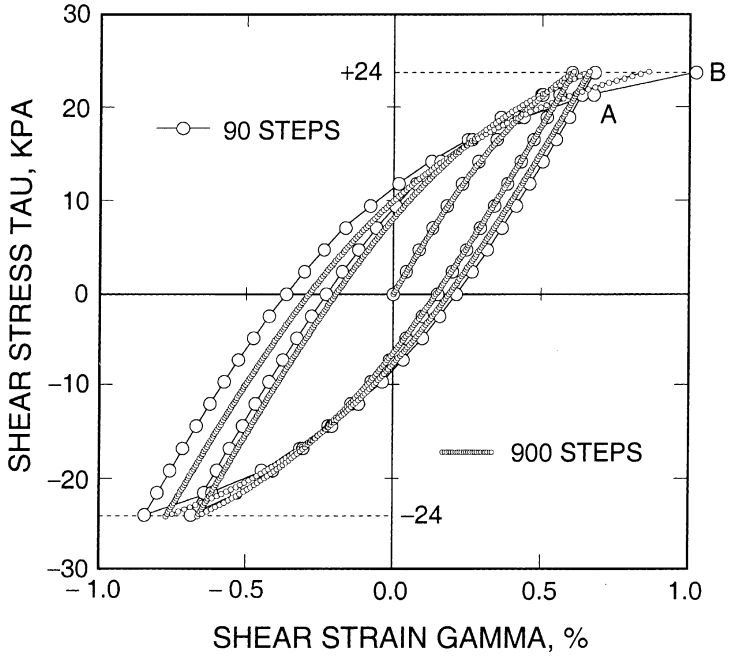

Fig. 15. Shear stress–shear strain curve for stress-controlled cyclic simple shearing ($h = 5$ MPa).

the local iterations are tabulated in the columns that correspond to the specific global iteration numbers. The asymptotic quadratic convergence of both the local and global iterations exhibited by the solution validate the consistent Jacobian and tangent operator developed for this bounding surface model. For the record the error tolerance used in the examples described in Sections 7.1–7.5 is 10^{-12} in both the local and global iteration levels based on the initial value of the residual norm.

7.6. FE analysis of strip footing

As a final example, we consider a finite element analysis of a strip footing on lightly overconsolidated clay. The finite element mesh for this problem is shown in Fig. 16 and consists of 717 nodes and 1344

Table 2
Convergence profile of Newton iterations for final load step of 90-step stress-controlled cyclic simple shearing example[a]

Global iteration number					
(1)	(2)	(3)	(4)	(5)	(6)
2.40e+0	**2.00e+0**	**4.37e−1**	**3.19e−2**	**1.82e−4**	**5.77e−8**
2.79e+2	2.05e+3	2.82e+3	2.88e+3	2.88e+3	2.88e+3
9.60e+0	2.77e+3	4.34e+2	4.47e+2	4.47e+2	4.47e+2
1.04e−2	8.12e+0	1.89e+1	2.00e+1	2.00e+1	2.00e+1
1.12e−9	4.14e−3	2.57e−2	2.92e−2	2.92e−2	2.92e−2
–	2.74e−9	1.07e−7	1.36e−7	1.36e−7	1.36e−7
	–	–	–	–	–

[a] *Note*: Bold-faced numbers pertain to residual norms of global iterations; light-faced numbers pertain to local iterations.

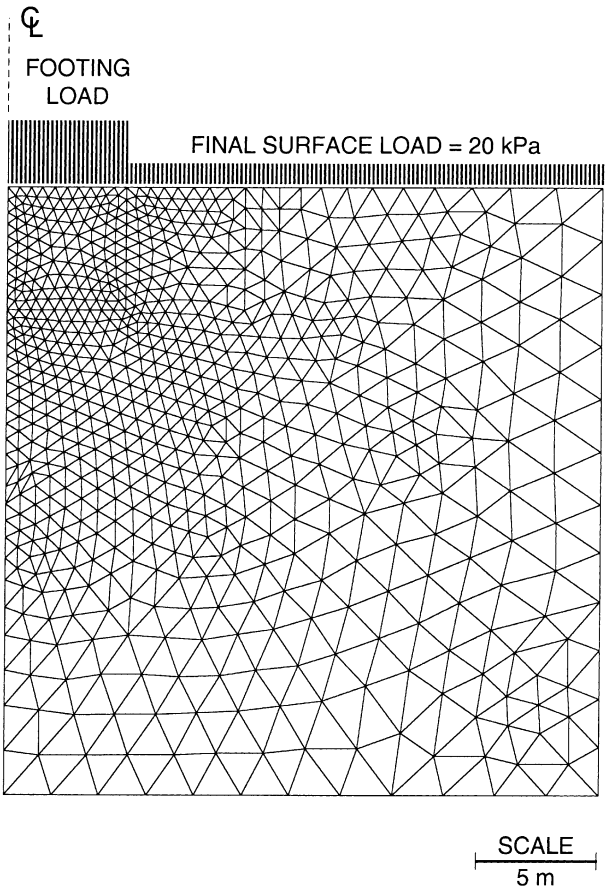

Fig. 16. Undeformed finite element mesh for strip footing example.

constant strain triangular elements deforming in plane strain. The parameters of the model are the same as in Section 7.1 and are summarized as follows: ellipsoidal axis ratio $c = 1.0$; hyperelastic compressibility parameter $\widetilde{\kappa} = 0.018$; elastic shear modulus $\mu_0 = 5.4$ MPa; hyperelastic parameter $\widetilde{\alpha} = 0$; compressibility parameter $\widetilde{\lambda} = 0.13$; and hardening parameter $m = 1.5$. Implied in the solution is that all loads are applied very slowly to allow the clay to consolidate at each load step.

A key part of the analysis involves establishing a realistic initial condition prior to the application of the footing load. Initial stresses are induced by gravity loads arising from the soil's own weight. In addition,

clay deposits are typically overconsolidated near the ground surface and normally consolidated at greater depths. To establish this initial condition we take a reference value of $\epsilon^{e}_{v0} = 0$ and $p_0 = -50$ kPa, and set $\boldsymbol{\epsilon}^{e} = \mathbf{0}$ initially at all Gauss points. This results in artificial low isotropic stress values of $\sigma_{11} = \sigma_{22} = \sigma_{33} = -50$ kPa at the Gauss points to get the solution started (note that it is not possible to start the analysis from a condition of zero initial stress since the elastic bulk modulus is a linear function of the mean normal stress). Body forces equivalent to a unit weight of $\gamma = 20$ kN/m^3 as well as surface preloads of 100 kPa are then applied to consolidate the soil. Finally, 80 kPa of the surface preload is removed to bring the soil to an initially overconsolidated state. Prototype stress paths representing this load history are shown in Fig. 17(a) and (b).

Having established this initial condition, a uniformly distributed footing load is applied in small increments up to failure, as shown in Fig. 17(c) for a prototype Gauss point. This essentially entails bringing the stress point to critical state line. Plots of total applied footing load versus centerline ground displacement are shown in Fig. 18 for three different values of the exponential hardening parameter h: 1, 5, and 100 MPa. The largest value of h, which results in a nearly hyperelastic response inside the bounding surface, exhibits a slightly concave upward curvature up until the bounding surface is reached. This is due to the stiffening effect in volumetric behavior of the soil under the footing with increasing mean normal stress. Fig. 18 also shows the bearing capacity slightly decreasing with decreasing values of h due to the reduction in soil shear strength with plasticity inside the bounding surface, a feature that is consistent with the stress paths for a previous example shown in Fig. 9. The deformed mesh, illustrated in Fig. 19, reveals settlement induced primarily by plastic volumetric compaction with little or no surface bulging.

Table 3 illustrates the strong convergence profiles of global Newton iterations, where quadratic convergence is achieved in all load steps up until the point of bearing capacity failure. For the record, the global

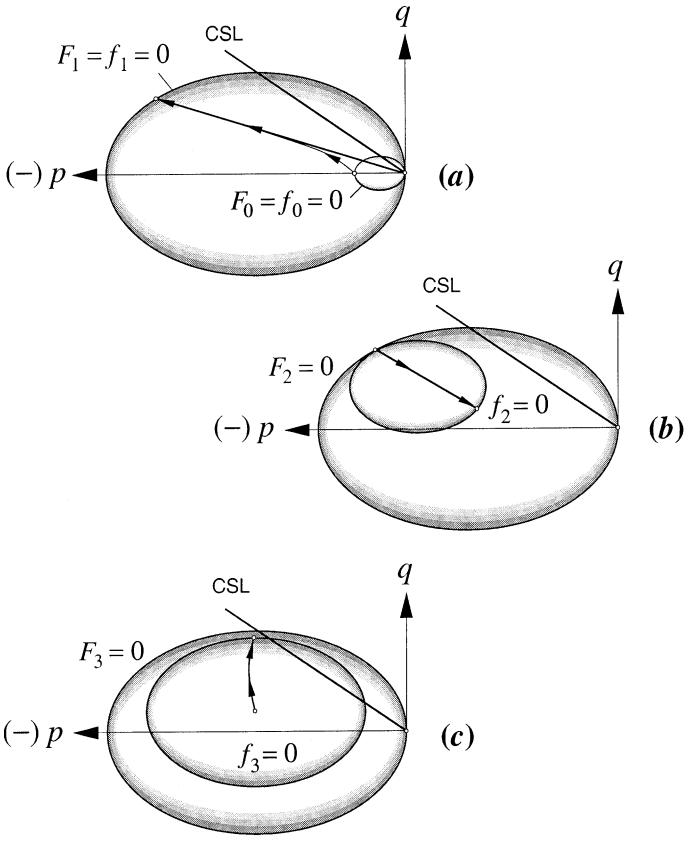

Fig. 17. Prototype stress paths at a Gauss point for strip footing problem: (a) gravity and surface preloading; (b) partial removal of surface preload; (c) application of footing load.

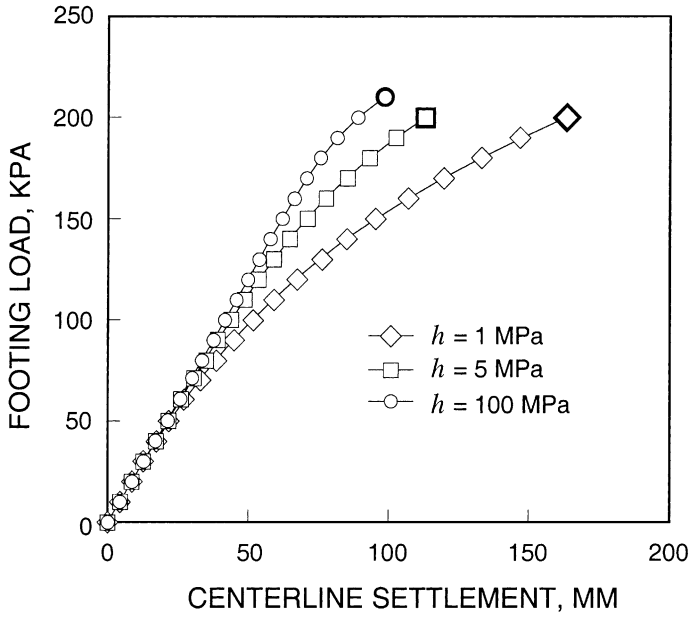

Fig. 18. Load–settlement response of strip footing on lightly overconsolidated clay. Note: Accented symbols denote last convergent load step.

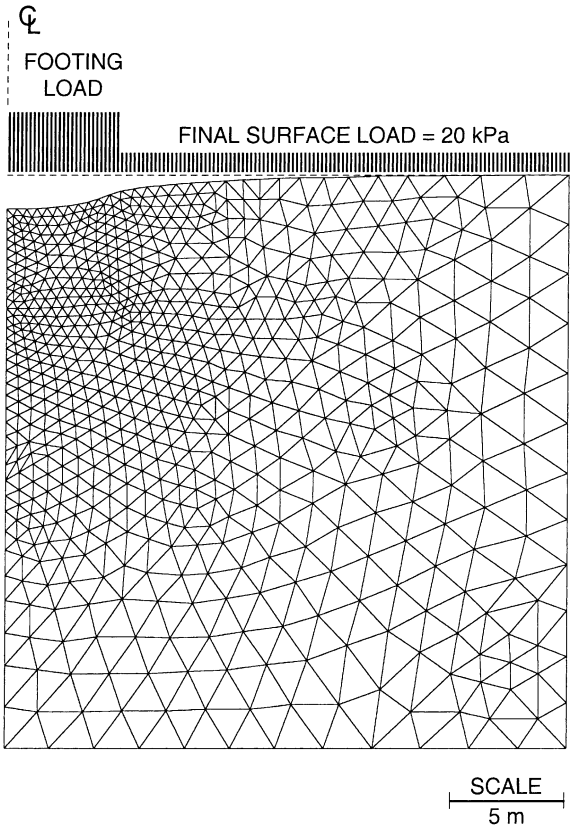

Fig. 19. Deformed finite element mesh for strip footing example ($h = 1$ MPa; displacement magnification factor = 10).

Table 3
Strip footing problem: convergence profile of global Newton iterations for final four convergent load increments ($h = 1$ MPa)[a]

Iteration number	Step number			
	(16)	(17)	(18)	(19)
0	1.00e+0	1.00e+0	1.00e+0	1.00e+0
1	8.00e−1	8.35e−1	8.61e−1	9.87e−1
2	7.10e−2	8.20e−2	8.06e−2	6.37e−2
3	6.89e−4	1.02e−3	1.19e−3	6.86e−3
4	9.30e−8	2.24e−7	4.89e−7	9.09e−6
5	4.21e−13	5.09e−13	6.82e−13	2.59e−11

[a] *Notes*: (a) Residual norms are normalized with respect to initial values. (b) Step #20 did not converge after 10 iterations.

Newton iterations are required to satisfy an error tolerance of 10^{-10} based on the initial norm of the nodal residual force vector. An important feature of the solution algorithm is a simple line search based on the majorization principle [41] and employing the quadratic interpolation polynomial as presented in [42]. Without this feature the iterations would not have converged in some of the critical loading steps, including the initial stages of gravity load imposition.

8. Summary and conclusions

A fully implicit stress-point integration algorithm for a class of anisotropic bounding surface plasticity models with ellipsoidal loading function has been presented. A key feature of the integration algorithm for the combined model is a return mapping in strain space, which allows fully implicit integration and consistent linearization of the constitutive equations. The consistency condition on the bounding surface is shown to be mathematically equivalent to the consistency condition on the loading surface for this class of models, thus allowing practically all attributes of the standard return mapping algorithm of classical plasticity theory to be carried over to the bounding surface theory with little modification. As a specific example, the infinitesimal version of modified Cam-Clay theory has been used to represent the bounding surface model. The algorithm is shown to perform very well under normal conditions in which the stress points are located on the compactive side of the critical state line. Work is now underway to enhance the robustness of the algorithm to handle just as effectively the softening response on the dilative side of the critical state line.

Acknowledgements

Financial support for this research was provided by the Earthquake Hazard Mitigation Division of National Science Foundation under Contract No. CMS-9613906, through the program of Dr. Clifford J. Astill. This support is gratefully acknowledged.

Appendix A. Reduced system for local integration algorithm

The size of the nonlinear system for the local integration algorithm can be reduced to eight by substituting $\widetilde{R}$ and $\widetilde{r}$ directly in the homology relation $R = (1 + \kappa)r$, thus eliminating R and r from the list of unknowns. Let us re-define the generalized residuals and unknowns as

$$\boldsymbol{b} = \begin{Bmatrix} \boldsymbol{b}_1 \\ b_2 \\ b_3 \end{Bmatrix} = \begin{Bmatrix} \boldsymbol{\epsilon}^{\mathrm{e}} - \boldsymbol{\epsilon}^{\mathrm{e\,tr}} + \Delta\gamma \boldsymbol{f} \\ \widetilde{R}(\boldsymbol{\epsilon}^{\mathrm{e}}) - (1 + \kappa)\widetilde{r}(\boldsymbol{\epsilon}^{\mathrm{e}}, \kappa) \\ f \end{Bmatrix}, \quad \boldsymbol{x} = \begin{Bmatrix} \boldsymbol{\epsilon}^{\mathrm{e}} \\ \kappa \\ \Delta\gamma \end{Bmatrix}. \tag{A.1}$$

The consistent Jacobian of the residuals can be written as

$$\boldsymbol{A}^k = \begin{bmatrix} \boldsymbol{A}_{11} & \boldsymbol{A}_{12} & \boldsymbol{A}_{13} \\ \boldsymbol{A}_{21} & A_{22} & A_{23} \\ \boldsymbol{A}_{31} & A_{32} & A_{33} \end{bmatrix}. \tag{A.2}$$

Individually, we have, for the linearization of $\boldsymbol{b}_1$,

$$\begin{aligned} \boldsymbol{A}_{11} &= \boldsymbol{I} + \Delta\gamma \boldsymbol{\phi} : \boldsymbol{c}^{\mathrm{e}} - \Delta\gamma \frac{\rho}{R} \boldsymbol{\phi} : (\boldsymbol{\alpha} \otimes \mathbf{1}), \\ \boldsymbol{A}_{12} &= -\frac{\Delta\gamma R}{(1+\kappa)^2} \boldsymbol{\phi} : (\boldsymbol{\Sigma}_0 + \mathbf{1}/c), \quad \boldsymbol{A}_{13} = \boldsymbol{f}. \end{aligned} \tag{A.3}$$

Linearizing b_2, we have

$$\boldsymbol{A}_{21} = [\rho - (1+\kappa)\eta]\mathbf{1}, \quad A_{22} = (1+\kappa)v - r, \quad A_{23} = 0, \tag{A.4}$$

where ρ, η, and v are defined in (6.13). Finally, linearizing b_3 gives

$$\begin{aligned} \boldsymbol{A}_{31} &= \boldsymbol{f} : \boldsymbol{c}^{\mathrm{e}} - \frac{\rho}{R} \boldsymbol{f} : (\boldsymbol{\alpha} \otimes \mathbf{1}) - 2\eta r \mathbf{1}, \\ A_{32} &= 2rv - \frac{r}{1+\kappa} \boldsymbol{f} : (\boldsymbol{\Sigma}_0 + \mathbf{1}/c), \quad A_{33} = 0. \end{aligned} \tag{A.5}$$

This is the actual iterative form implemented in the local integration algorithm.

Appendix B. Elastic tangential compliance tensor

The elastic tangential compliance tensor, $\boldsymbol{d}^{\mathrm{e}} = \boldsymbol{c}^{\mathrm{e}-1}$, can be evaluated in closed form provided that the matrix $\boldsymbol{D}^{\mathrm{e}}$ relating the rates of stress and strain invariants is invertible, i.e.,

$$\begin{Bmatrix} \dot{\epsilon}_v^{\mathrm{e}} \\ \dot{\epsilon}_s^{\mathrm{e}} \end{Bmatrix} = \boldsymbol{E}^{\mathrm{e}} \begin{Bmatrix} \dot{p} \\ \dot{q} \end{Bmatrix}, \quad \boldsymbol{E}^{\mathrm{e}} = \boldsymbol{D}^{\mathrm{e}-1} = \begin{bmatrix} E_{11}^{\mathrm{e}} & E_{12}^{\mathrm{e}} \\ E_{12}^{\mathrm{e}} & E_{22}^{\mathrm{e}} \end{bmatrix}. \tag{B.1}$$

As indicated in Section 4, the inverse of $\boldsymbol{D}^{\mathrm{e}}$ exists provided that the stress ratio q/p does not reach a certain maximum value.

Assuming that $\boldsymbol{D}^{\mathrm{e}-1}$ exists, the elastic compliance tensor can be obtained from the elastic strain tensor decomposition

$$\boldsymbol{\epsilon}^{\mathrm{e}} = \frac{1}{3}\epsilon_v^{\mathrm{e}} \mathbf{1} + \sqrt{\frac{3}{2}} \epsilon_s^{\mathrm{e}} \hat{\boldsymbol{n}}, \tag{B.2}$$

where $\hat{\boldsymbol{n}} = \boldsymbol{e}^{\mathrm{e}}/\|\boldsymbol{e}^{\mathrm{e}}\| = \boldsymbol{s}/\|\boldsymbol{s}\|$. Taking the time-derivative gives

$$\dot{\boldsymbol{\epsilon}}^{\mathrm{e}} = \frac{1}{3}\dot{\epsilon}_v^{\mathrm{e}} \mathbf{1} + \sqrt{\frac{3}{2}} \dot{\epsilon}_s^{\mathrm{e}} \hat{\boldsymbol{n}} + \sqrt{\frac{3}{2}} \epsilon_s^{\mathrm{e}} \dot{\hat{\boldsymbol{n}}}, \tag{B.3}$$

where

$$\dot{\hat{\boldsymbol{n}}} = \frac{1}{\|\boldsymbol{s}\|} \left(\boldsymbol{I} - \frac{1}{3}\mathbf{1} \otimes \mathbf{1} + \hat{\boldsymbol{n}} \otimes \hat{\boldsymbol{n}} \right) : \dot{\boldsymbol{\sigma}}. \tag{B.4}$$

Substituting (B.1) into (B.3), and using the identities

$$\dot{p} = \frac{1}{3}\mathbf{1} : \dot{\boldsymbol{\sigma}}, \quad \dot{q} = \sqrt{\frac{3}{2}} \hat{\boldsymbol{n}} : \dot{\boldsymbol{\sigma}}, \quad \dot{\boldsymbol{s}} = \left(\boldsymbol{I} - \frac{1}{3}\mathbf{1} \otimes \mathbf{1} \right) : \dot{\boldsymbol{\sigma}} \tag{B.5}$$

results in the inverse rate-constitutive equation

$$\dot{\boldsymbol{\epsilon}}^{\mathrm{e}} = \boldsymbol{d}^{\mathrm{e}} : \dot{\boldsymbol{\sigma}}. \tag{B.6}$$

where

$$\boldsymbol{d}^{\mathrm{e}} = \frac{3}{2} D_{22}^{\mathrm{e}-1} \boldsymbol{I} + \left(\frac{1}{9} E_{11}^{\mathrm{e}} - \frac{1}{2} D_{22}^{\mathrm{e}-1} \right) \mathbf{1} \otimes \mathbf{1} + \frac{1}{\sqrt{6}} E_{12}^{\mathrm{e}} (\mathbf{1} \otimes \hat{\boldsymbol{n}} + \hat{\boldsymbol{n}} \otimes \mathbf{1}) + \frac{3}{2} \left(E_{22}^{\mathrm{e}} - D_{22}^{\mathrm{e}-1} \right) \hat{\boldsymbol{n}} \otimes \hat{\boldsymbol{n}}. \tag{B.7}$$

One can easily verify that $\boldsymbol{c}^{\mathrm{e}} : \boldsymbol{d}^{\mathrm{e}} = \boldsymbol{d}^{\mathrm{e}} : \boldsymbol{c}^{\mathrm{e}} \equiv \boldsymbol{I}$.

References

[1] R.I. Borja, H.Y. Chao, F.J. Montáns, C.H. Lin, Nonlinear ground response at Lotung LSST site, J. Geotech. Geoenviron. Engrg. ASCE 125 (1999) 187–197.

[2] R.I. Borja, H.Y. Chao, F.J. Montáns, C.H. Lin, SSI effects on ground motion at Lotung LSST site, J. Geotech. Geoenviron. Engrg. ASCE 125 (1999) 760–770.

[3] R.I. Borja, C.H. Lin, K.M. Sama, G.M. Masada, Modelling non-linear ground response on non-liquefiable soils, Earthquake Engrg. Struct. Dyn. 29 (2000) 63–83.

[4] W.D. Iwan, On a class of models for the yielding behavior of continuous and composite systems, J. Appl. Mech. Trans. ASME 34 (E3) (1967) 612–617.

[5] Z. Mróz, On the description of anisotropic work hardening, J. Mech. Phys. Solids, London 15 (1967) 163–175.

[6] J.H. Prevost, Mathematical modelling of monotonic and cyclic undrained clay behavior, Int. J. Numer. Analyt. Methods Geomech. 1 (1977) 195–216.

[7] J.H. Prevost, Anisotropic undrained stress–strain behavior of clays, J. Geotech. Engrg. Div. ASCE 104 (1978) 1075–1090.

[8] Z. Mróz, V.A. Norris, O.C. Zienkiewicz, Application of an anisotropic hardening model in the analysis of elasto-plastic deformation of soils, Géotechnique 29 (1979) 1–34.

[9] Y.F. Dafalias, E.P. Popov, Cyclic loading for materials with a vanishing elastic region, Nucl. Engrg. Des. 41 (1977) 293–302.

[10] Y.F. Dafalias, L.R. Herrmann, Bounding surface formulation of soil plasticity, in: G.N. Pande, O.C. Zienkiewicz (Eds.), Chapter 10: Soil Mechanics – Transient and Cyclic Loads, Wiley, New York, 1982, pp. 253–282.

[11] Y.F. Dafalias, Bounding surface plasticity, I: Mathematical foundation and hypoplasticity, J. Engrg. Mech. ASCE 112 (1986) 966–987.

[12] Y.F. Dafalias, L.R. Herrmann, Bounding surface plasticity, II: Application to isotropic cohesive soils, J. Engrg. Mech. ASCE 112 (1986) 1263–1291.

[13] J.P. Bardet, Bounding surface plasticity model for sand, J. Engrg. Mech. ASCE 116 (1986) 983–1001.

[14] R.S. Crouch, J.P. Wolf, Unified 3D critical state bounding-surface plasticity model for soils incorporating continuous plastic loading under cyclic paths. Part I: Constitutive relations, Int. J. Numer. Analyt. Methods Geomech. 18 (1994) 735–758.

[15] R.S. Crouch, J.P. Wolf, Unified 3D critical state bounding-surface plasticity model for soils incorporating continuous plastic loading under cyclic paths. Part II: Calibration and simulations, Int. J. Numer. Analyt. Methods Geomech 18 (1994) 759–784.

[16] T.J.R. Hughes, Numerical implementation of constitutive models: rate independent deviatoric plasticity, in: S. Nemat-Nasser, R. Asaro, G. Hegemier (Eds.), Theoretical Foundations for Large-Scale Computations of Nonlinear Material Behaviour, Martinus Nijhoff, The Netherlands, 1984.

[17] M. Ortiz, J.B. Martin, Symmetry-preserving return mapping algorithms and incrementally extremal paths: a unification of concepts, Int. J. Numer. Methods Engrg. 28 (1989) 1839–1853.

[18] J.C. Simo, T.J.R. Hughes, Elastoplasticity and Viscoplasticity – Computational Aspects, Springer Series in Applied Mathematics, Springer, Berlin, 1989.

[19] J.J. Moreau, Application of convex analysis to the treatment of elasto-plastic systems, in: P. Germain, B. Nayroles (Eds.), Applications of Methods of Functional Analysis to Problems in Mechanics, Springer, Berlin, 1976.

[20] J.C. Simo, S. Govindjee, Nonlinear B-stability and symmetry preserving return mapping algorithms for plasticity and viscoplasticity, Int. J. Numer. Methods Engrg. 31 (1991) 151–176.

[21] J.C. Simo, On the computational significance of the intermediate configuration and hyperelastic stress relations in finite deformation elastoplasticity, Mech. Mater. 4 (1985) 439–451.

[22] J.C. Simo, T.J.R. Hughes, General return mapping algorithms for rate-independent elastoplasticity, in: C.S. Desai et al. (Eds.), Constitutive Laws for Engineering Materials: Theory and Applications, Elsevier Science, New York, 1987, pp. 221–231.

[23] R.I. Borja, C. Tamagnini, Cam-Clay plasticity, Part III: Extension of the infinitesimal model to include finite strains, Comput. Methods Appl. Mech. Engrg. 155 (1998) 73–95.

[24] L.R. Herrmann, V. Kaliakin, C.K. Shen, K.D. Mish, Z.Y. Zhu, Numerical implementation of plasticity model for cohesive soils, J. Engrg. Mech. ASCE 113 (1987) 500–519.

[25] R.I. Borja, A.P. Amies, Multiaxial cyclic plasticity model for clays, J. Geotech. Engrg. ASCE 120 (1994) 1051–1070.

[26] M. Kojic, Elastic–plastic analysis of soil using bounding surface Cam-Clay model, in: D.R.J. Owen, E. Oñate, E. Hinton (Eds.), Computational Plasticity Fundamentals and Applications, CIMNE Barcelona, Spain, 1997, pp. 1691–1695.

[27] M.T. Manzari, M.A. Nour, On implicit integration of bounding surface plasticity models, Comput. Struct. 63 (1997) 385–395.

[28] K.H. Roscoe, J.H. Burland, On the generalized stress–strain behavior of 'wet' clay, in: J. Heyman, F.A. Leckie (Eds.), Engineering Plasticity, Cambridge University Press, Cambridge, 1968, pp. 535–609.

[29] A. Schofield, P. Wroth, Critical State Soil Mechanics, McGraw-Hill, New York, 1968.

[30] R.I. Borja, S.R. Lee, Cam-Clay plasticity, Part I: Implicit integration of elasto-plastic constitutive relations, Comput. Methods Appl. Mech. Engrg. 78 (1990) 49–72.
[31] R.I. Borja, Cam-Clay plasticity, Part II: Implicit integration of constitutive equation based on a nonlinear elastic stress predictor, Comput. Methods Appl. Mech. Engrg. 88 (1991) 225–240.
[32] A.M. Britto, M.J. Gunn, Critical State Soil Mechanics via Finite Elements, Wiley, New York, 1987.
[33] A. Gens, D.M. Potts, Critical state models in computational geomechanics, Engrg. Comput. 5 (1988) 178–197.
[34] M. Zytynski, M.K. Randolph, R. Nova, C.P. Wroth, On modeling the unloading–reloading behaviour of soils, Int. J. Numer. Analyt. Methods Geomech. 2 (1978) 87–93.
[35] G.T. Houlsby, The use of a variable shear modulus in elastic–plastic models for clays, Comput. Geotech. 1 (1985) 3–13.
[36] R. Butterfield, A natural compression law for soils, Géotechnique 29 (1979) 469–480.
[37] K. Hashiguchi, M. Ueno, Elasto-plastic constitutive laws of granular materials, in: S. Murayama, A.N. Schofield (Eds.), Constitutive Equations of Soils, Proceedings of the Ninth International Conference on Soil Mechanics and Foundation Engineering, Specialty Session 9, Tokyo, 1977, pp. 73–82.
[38] K. Hashiguchi, On the linear relations of $V - \ln p$ and $\ln v - \ln p$ for isotropic consolidation of soils, Int. J. Numer. Analyt. Methods Geomech. 19 (1995) 367–376.
[39] R.I. Borja, C. Tamagnini, A. Amorosi, Coupling plasticity and energy-conserving elasticity models for clays, J. Geotech. Geoenviron. Engrg. ASCE 123 (1997) 948–957.
[40] T.W. Lambe, R.V. Whitman, Soil Mechanics, Wiley, New York, 1969.
[41] J.M. Ortega, W.C. Rheinboldt, Iterative Solution of Nonlinear Equations in Several Variable, Academic Press, New York, 1970.
[42] R.I. Borja, Composite Newton-PCG and quasi-Newton iterations for nonlinear consolidation, Comput. Methods Appl. Mech. Engrg. 86 (1991) 27–60.